The Thesis Committee for Micaela Nicole Pedrazas Hinojosa certifies that this is the approved version of the following Thesis:

Ice-free lagoon sediment in areas of continuous Arctic permafrost revealed through electrical resistivity imaging

MAY 2020

APPROVED BY
SUPERVISING COMMITTEE:

Meinhard Bayani Cardenas, Supervisor

James W. McClelland

Daniella M. Rempe

Ice-free lagoon sediment in areas of continuous Arctic permafrost revealed through electrical resistivity imaging

by

Micaela Nicole Pedrazas Hinojosa

Thesis

Presented to the Faculty of the Graduate School of

The University of Texas at Austin

in Partial Fulfillment

of the Requirements

for the Degree of

Master of Science in Geological Sciences

The University of Texas at Austin

May 2020

Dedication

I dedicate my thesis work to my loving parents, Albaro Pedrazas and Vivian Hinojosa, whose words of encouragement and push for tenacity ring in my ears. My twin sister, Michelle Pedrazas, who accompanies me so intentionally through every stage of my life and my brother, Diego Pedrazas, who is so special to me. My rock, Ryker Harger, who has faithfully been there for me through this process. I also dedicate this thesis to my friends, both in Bolivia and the US, with a special shout out to my hydro-fam, who have encouraged and supported me. I am especially thankful to my mentor, Bayani Cardenas, for knowing how to lead and care for our research group.

Lastly, I dedicate this and all my future endeavors to JMJ.

Acknowledgements

This work was supported by the Geology Foundation at the University of Texas at Austin. We thank the U.S. Fish and Wildlife Service for logistical support and for permits to conduct research within the lagoon. Resources were provided by the National Science Foundation through the Beaufort Lagoon Ecosystems LTER (award #1656026). Micaela Pedrazas was supported by a fellowship from the Ivanhoe Foundation, a student research grant from the Geological Society of America and an Off-Campus Research Award by the Jackson School of Geosciences. We are grateful to the Kaktovik Inupiat Corporation for allowing us to carry out field work on their land. Micaela Pedrazas, Bayani Cardenas and Jim McClelland designed the studies. Micaela Pedrazas, Bayani Cardenas, Jim McClelland, Jeff Watson, Craig Connolly, Cansu Demir and Nathan Sonderman conducted field work. Micaela Pedrazas conducted the resistivity data processing, created the figures and wrote the thesis with guidance from Bayani Cardenas. All committee members provided input during the writing of the thesis. Micaela Pedrazas declares no conflicting financial interests.

Abstract

Ice-free lagoon sediment in areas of continuous Arctic permafrost revealed through electrical resistivity imaging

Micaela Nicole Pedrazas Hinojosa, M.S.Geo.Sci

The University of Texas at Austin, 2020

Supervisor: Meinhard Bayani Cardenas

The Arctic is undergoing profound changes due to amplification of global warming in northern latitudes. One of the key features in the Arctic that remains understudied is ice-bonded subsea permafrost. This coastal feature is assumed to be ice-rich and underlies the many coastal lagoons in the Arctic. Subsea permafrost, is estimated to store as much organic carbon as Earth's atmosphere and protects Arctic coastlines from erosion. However, subsea frozen sediment near the shoreline has not been thoroughly mapped and how much thawed sediment exists beneath coastal lagoons remains unclear. The presence or absence of ice beneath the surface, and its thawing are vital information that potentially represent a positive carbon feedback to the global climate system. Through modeling and direct observations of electrical resistivity across a lagoon on the Alaska Beaufort Sea coast during the summer, we found that the subsurface is ice-free down to at least 17 m under the lagoon and down to 22 m at the beach. This finding contrasts with the broadly held idea of continuity of ice-rich permafrost across the land-sea interface extending from land to offshore in the near-surface. Since the subsurface beneath the beach

and the lagoon are unfrozen to depths of at least ~ 20 m, there exists a significantly thawed portion of sediment beneath the lagoons, which may serve as a source and conduit for heat, water, and carbon exchange.

Table of Contents

List of Tables

List of Figures

Chapter 1: Introduction

1.1 MOTIVATION

Permafrost is defined as sediment persisting at or below 0°C for at least two consecutive years and exists both on land (terrestrial permafrost) and underwater (subsea permafrost). There is extensive relict subsea permafrost in the Arctic. A GIS-based study estimated that the likely area of the northern permafrost today is 23.6 million km^2 with approximately 2.4 million km^2 remaining underwater as subsea permafrost, also known as sea shelf permafrost (Lindgren, Hugelius, Kuhry, Christensen, & Vandenberghe, 2016) (Figure 1).

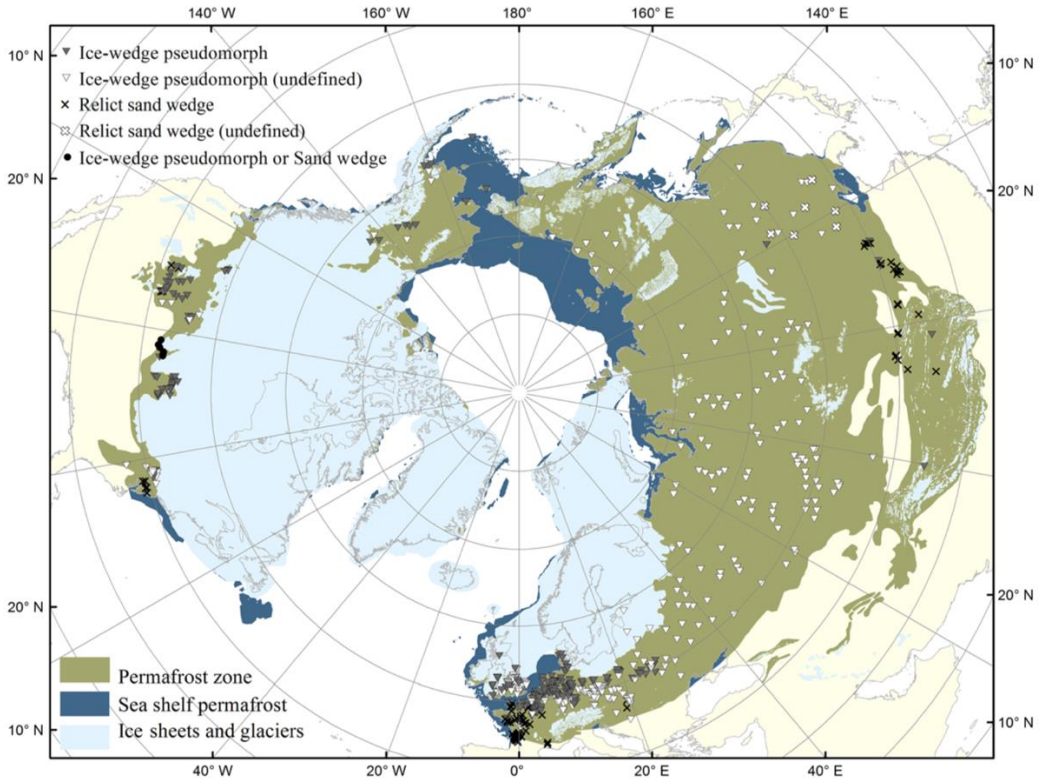

Figure 1: Permafrost zones, sea shelf permafrost and glaciers (Lindgren et al., 2016).

This spatial extent agrees with another study that used geophysical well logs, to estimate the current extent of subsea permafrost to be 2.3 million km^2 (Mu et al., 2019). Using paleo records, scientists have estimated that sea level during the Pleistocene was approximately 120 m lower than it is today (Figure 2). This sea level rise submerged continental shelves around the globe, including millions of square kilometers of Arctic terrestrial permafrost, resulting in underwater subsea permafrost.

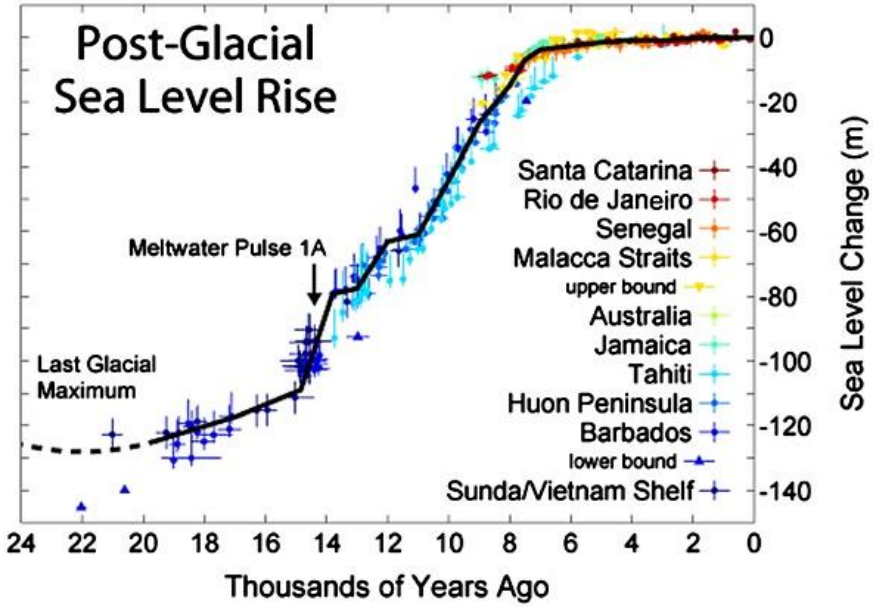

Figure 2: Sea level rise after the Last Glacial Maximum (Moore, Grinsted, Zwinger, & Jevrejeva, 2013).

Studies have shown that this submerged permafrost is a massive storehouse for ancient carbon which remains trapped within its cryotic structure. The on-going thaw and degradation of subsea permafrost has far-reaching effects,

but perhaps none more important than the mobilization of ancient carbon and subsequent release of carbon dioxide and methane, which has the potential to exacerbate global warming (Hugelius et al., 2014; Ruppel & Kessler, 2017).

For example, a model focusing on the organic carbon stored in just the top 25 m of subsea permafrost in the northern hemisphere, estimated that it contains 860 (± 590) Pg of organic carbon which is roughly the same amount of carbon as currently held in the atmosphere (Mu et al., 2019). In particular, the subsea permafrost table has been lowering at a rate of up to 14 cm/year in Eastern Siberia and at an average of 4 cm/year in the Beaufort Sea in Alaska (Overduin et al., 2012; Shakhova et al., 2017). The degradation of relict permafrost and its local effects are even more dramatic adjacent to the coast, where the connection to degrading permafrost on land is even stronger. Therefore, it is imperative to determine the extent of thawing of frozen subsea permafrost and the hydraulic "connection" between land and subsea permafrost.

As a consequence of subsea permafrost degradation, we can expect a greater transfer of heat between thawed underwater sediment and the frozen coast, potentially facilitating further coastal erosion. Thawing and collapsing Arctic coastlines can have erosion rates as high as 25 m/year, releasing 14 Tg of organic carbon annually into the near shore zones (Fritz, Vonk, & Lantuit, 2017). Locally, thaw-induced damage is profoundly felt by communities throughout the northern high latitude regions (Osterkamp, 2001).

Such is the case in our study area near the village of Kaktovik on Barter Island, a coastal indigenous community located in the continuous permafrost region of the Alaskan Beaufort Sea, whose subsistence and cultural identity is intricately connected with their environment. Kaktovik is within the Arctic coastal plain which is characterized by a low-relief tundra-covered surface underlain by continuous permafrost. Adjacent to Barter Island is Kaktovik Lagoon. Approximately 84% of Kaktovik Lagoon's coast is eroding (Gibbs & Richmond, 2017). The average coastal erosion rate is 0.6 m/yr and with a maximum rate of 4.5 m/yr for the period of 1947 to 2010. Kaktovik Lagoon's coastal retreat exposes terrestrial permafrost which then becomes inundated as subsea relict permafrost. This subsea permafrost would in turn continue to warm up and melt as coastal waters heat up and experience shorter and shorter periods of ice cover (Wendler, Shulski, & Moore, 2010). The distribution of ice on and beneath the land and lagoon is the primary factor determining the fate and vulnerability of the coastal carbon pool and the stability of coastlines, including Kaktovik's.

The Arctic coast of northeastern Alaska and northwestern Canada is lined with hundreds of kilometers of lagoon-barrier island systems. We studied one of these lagoons in the Alaskan Beaufort Sea (Figure 3).

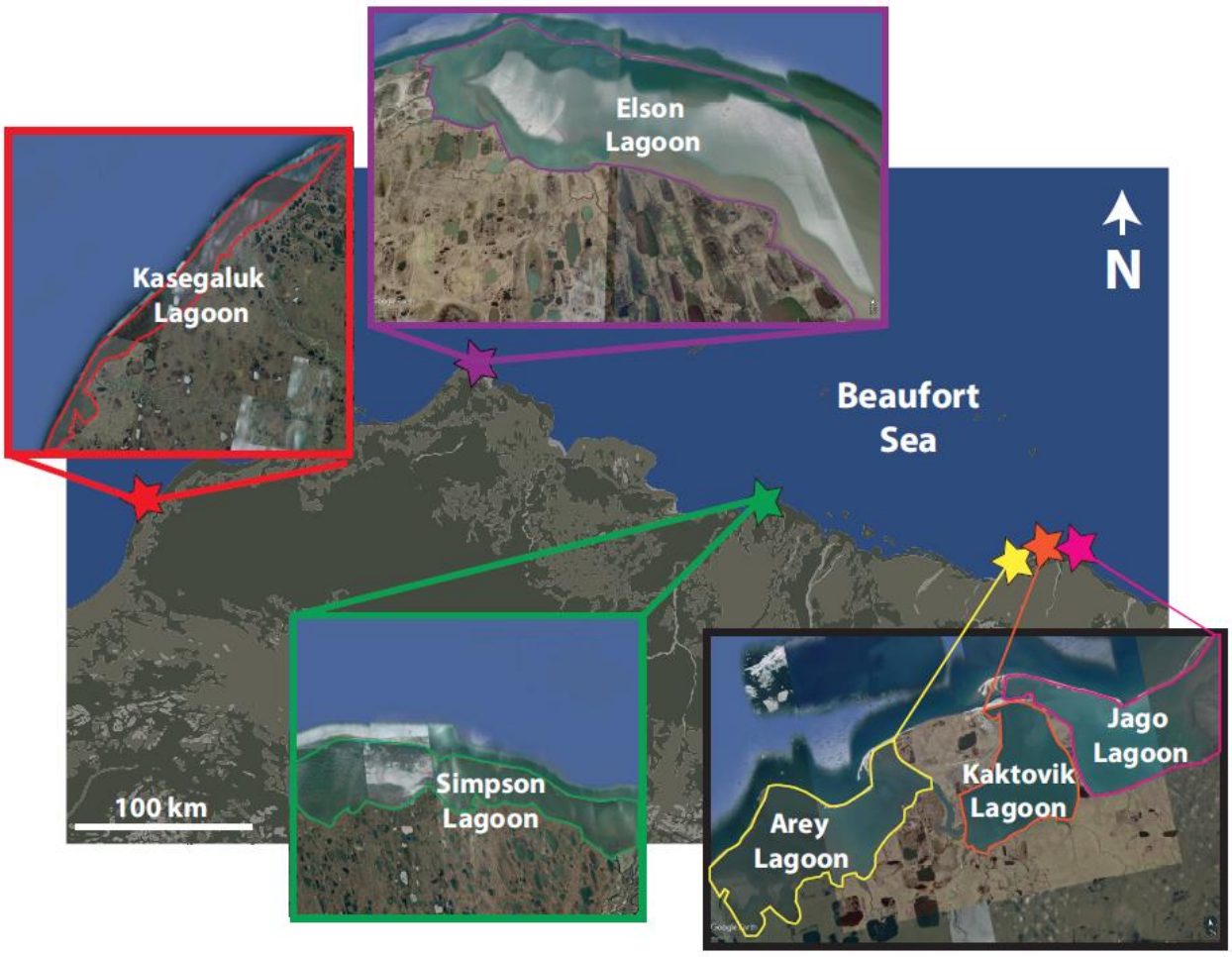

Figure 3: Exemplary lagoon-barrier systems along the Arctic coast. Kaktovik lagoon is highlighted by the orange star (latitude: 70.1015543°, longitude: -143.737702°).

1.2 Local Hydrology and Hydrogeology

Kaktovik Lagoon is located between the Okpilak and Jago River on the Beaufort Sea coast. The landward shores of Kaktovik Lagoon have narrow sandy

beaches, typically a few meters wide, which abut bluffs that vary in height but are typically 1-3 m high. The bluffs mark the beginning of the tundra with ice-wedge polygons. Ice-bearing permafrost within the polygons typically begins within a few decimeters beneath the surface. The boundaries of the polygons represent troughs which form a local connected network of surface channels (Figure 4) which drains a portion of groundwater from the polygons and delivers it to the beaches over the summer.

Freshwater enters Kaktovik Lagoon via three main sources: (1) two relatively larger streams on the southwestern and southeastern corners of the lagoon, which include a larger drainage area; (2) streams from the tundra which drain small thermokarst ponds and the very local networks of troughs in between ice-wedge polygons (Figure 4) ; and (3) groundwater flowing through interstices in surficial and deep porous soils, that extends into thawing permafrost and carries abundant dissolved organic carbon and nitrogen (Connolly, Cardenas, Burkart, Spencer, & McClelland, 2020).

Figure 4: Surface water entering the lagoon through two main mechanisms. (A) Two large streams that feed the lagoon and (B) streams from the tundra that that drain small thermokarst features.

Although the exchange with the Beaufort Sea is limited by the surrounding barrier islands, the lagoon exhibits hypersaline conditions driven by ice-formation and associated salt exclusion during fall/winter. The salty winter water is mostly flushed by freshwater from lagoon ice melt and runoff from land during spring, although some hypersaline conditions persists into summer in bottom waters (Dunton, Schonberg, & Cooper, 2012; Harris, McClelland,

Connelly, Crump, & Dunton, 2017). The shallow subsurface consists mostly of peat around the edges of the lagoon, and unconsolidated marine and non-marine silt- to gravel-sized sediment as seen from a borehole in the main island, Barter Island (latitude 70.116530° and longitude -143.628500°). Subsurface temperatures, although remaining below 0°C, continue to increase every year (Figure 5).

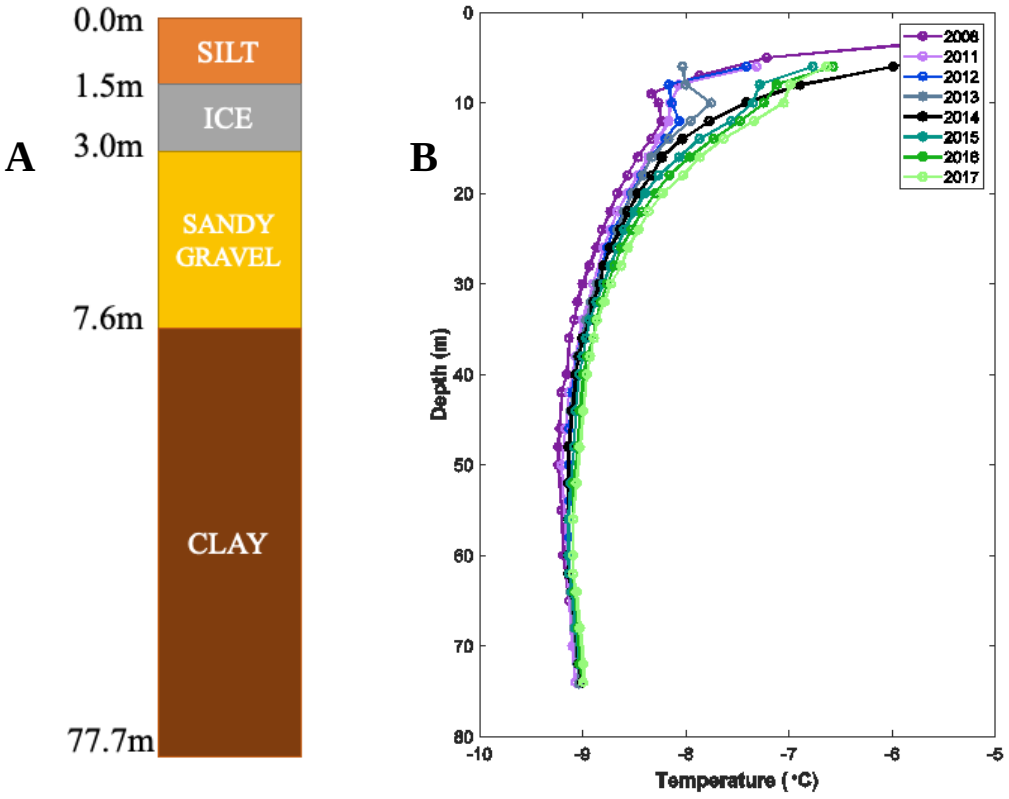

Figure 5: (A) Borehole in Barter Island indicating lithology (Osterkamp & Jorgenson, 2006). (B) Subsurface temperature plot for years 2008, 2011, 2012, 2013, 2014, 2015, 2016 and 2017 (source: https://permafrost.gi.alaska.edu/site/uf1).

1.3 HISTORICAL CONTEXT

Kaktovik is a village on Barter Island in North Slope Borough, Alaska within the Arctic National Wildlife Refuge (ANWR) that carries centuries of history for native Alaskan communities. As of 2010, the village has a population of 239 people and is recently becoming a touristic place due to the many polar bear sightings. However, up until the late 1800s, Barter Island was actually a major trade center for the Inupiat Alaskan natives and the Inuit from Canada. Kaktovik was traditionally a good fishing place, with no permanent settlers until the city was established in 1971 with the construction of a runway. Due to the island's remote location, community members take pride of maintaining Inupiat Eskimo traditions and continue to depend on subsistence fishing and hunting of whale, caribou, and seals.

Figure 6: Aerial view of Kaktovik and Barter Island LRRS by the US Fish and Wildlife.

Kaktovik's villagers, similar to most coastal communities in the North Slope of Alaska, are specially adapted to living in frigid temperatures and tundra environments. However, with warming ocean temperatures, a new Arctic landscape is emerging where frozen sediment is thawing both on land and underwater, lagoon open water is expanding and warm seasons are lasting longer. This creates new challenges for infrastructure, hunting, and preserving tradition (Cuomo, Eisner, & Hinkel, 2008).

1.4 Previous Study on Barter Island's Geomorphologic Evolution

Between 1947 and 2003, the coast of Barter Island was predominantly erosional except for accretion and extension of the spits to the East and West of the island. East of Barter Island the mainland coast of Jago Lagoon and the eastern two-thirds of Kaktovik Lagoon is characterized by moderately high tundra bluffs (about 2–4 m high) and narrow (<20 m wide) beaches. The sheltered mainland-lagoon coast between the Jago River Delta and Hulahula River Delta is predominantly erosional (84 % of transects) with an average shoreline change rate of -0.6 m/yr and range of -4.5 to +1.5 m/yr (Gibbs & Richmond, 2017) (Figure 7).

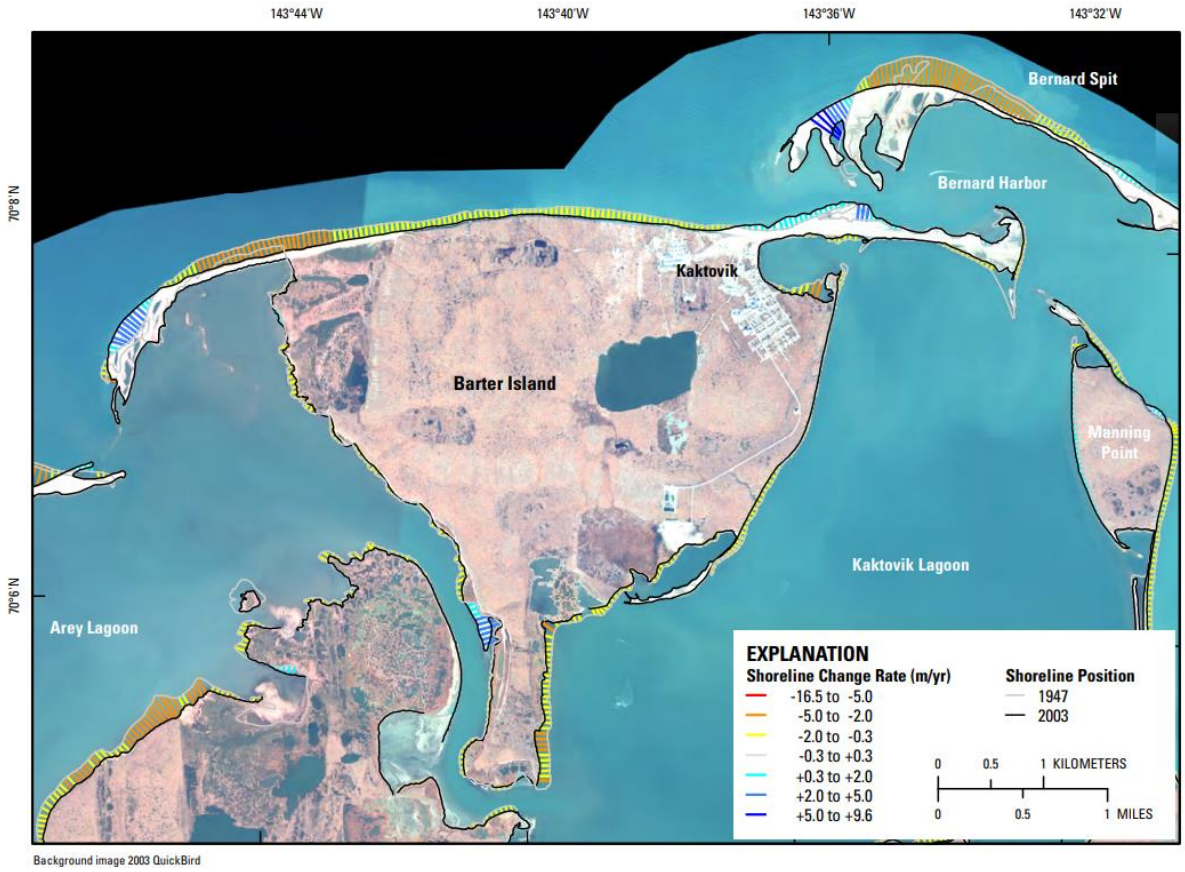

Figure 7: Map showing color-coded shoreline change rates for Barter Island on the North Slope, Beaufort Sea Coast of Alaska from Gibbs et al. (2018).

Erosion along permafrost coastal bluffs at Barter Island increased from 1.6 m yr^{-1} (1979–2003) to 5.5 m yr^{-1} (2003–2017), a 3.4-fold increase (Gibbs, Nolan, Richmond, Snyder, & Erikson, 2019). Coastal permafrost bluffs at Barter Island are among the most rapidly eroding along Alaska's coast, having retreated up to 132 m between 1955 and 2015 (Gibbs et al., 2019). Using photogrammetry from a manned aircraft and validating it with thousands of checkpoints, researchers

found that of the bluff material between 2014-15, (70%) was lost during the 3 summer months (July to Sept) of 2014 and the remaining 30% between the late-summer and following winter-spring (Gibbs et al., 2019).

1.5 RESEARCH PROBLEM

There is a pressing need to study subsea ice-bonded permafrost in Arctic coastal lagoons both from a local and global perspective. Globally, there are vast amounts of carbon that could be released when ice-bonded subsea permafrost degrades or when the coast erodes. Locally, there is an immediate need for information about the impacts of degrading subsea permafrost on the welfare, food security, land stability, cultural heritage, and economic growth of the community members (Cuomo et al., 2008; Fritz et al., 2017). Like many areas of the Arctic coast, the presence and dynamics of subsea ice-bearing permafrost within Kaktovik Lagoon has not been documented.

Direct observations made through drilling, probing and sampling are sparse, expensive and provide only limited point observations. Geophysical methods such as electromagnetic, seismic, and electrical resistivity (ER) have become widely used in identifying the distribution of terrestrial permafrost (Hauck, 2013; Olhoeft, 1975). However, there are far fewer investigations of subsea ice-bonded permafrost. Recent regional mapping efforts using seismic surveys to constrain the seaward extent of frozen subsea permafrost in the Alaskan Beaufort Sea begin relatively far offshore and ignore the lagoons and

near-shore zones where subsea permafrost is most vulnerable (Brothers, Herman, Hart, & Ruppel, 2016).

Coastal and offshore applications of electrical resistivity imaging (ERI) have emerged as a promising cost-effective geophysical method that can readily provide horizontally-continuous and depth-resolved images of the electrical properties of the subsurface (Cardenas et al., 2010; Swarzenski et al., 2016). This is particularly advantageous in remote areas, such as our study area, where drilling boreholes to acquire 1D lithological logs proves especially difficult or expensive. ERI introduces electrical current into the subsurface through a pair of current electrodes while measuring the electrical potential field simultaneously using pairs of voltage electrodes (Figure 8). The premise is based on how much subsurface materials resist current flow, essentially treating the subsurface like a network of resistors. Ice and frozen sediment impede current more than unfrozen, conductive sediment. Electrical resistivity (ER) generally increases exponentially with increasing ice content making this method particularly useful to differentiate between frozen and unfrozen sediment (Pearson, Halleck, McGuire, Hermes, & Mathews, 1983).

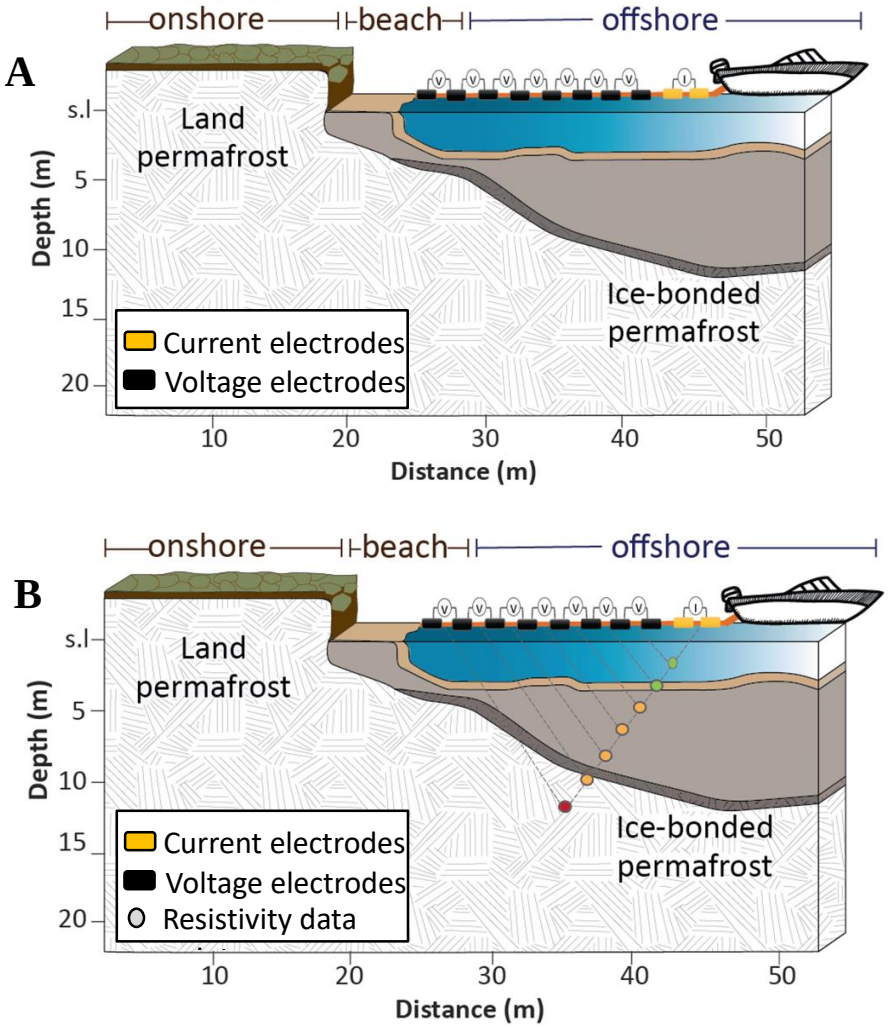

Figure 8: Electrical resistivity imaging. (A) Boat towing floating electrodes across water body. (B) Current electrodes introducing current into the subsurface and voltage electrodes record the response of the subsurface as apparent resistivity data points.

The fundamental equation relating resistance measured to the current injected is based on Ohm's law:

$$R=V/I$$ **Equation 1:** Ohm's Law.

Where, R (Ω) denotes resistance

V (V), denotes voltage

I (A), denotes current

From this resistance measurement, we can apply a geometric factor to take into account the nature of the material and calculate the material property of apparent resistivity, ρa measured in Ωm.

Apparent resistivity is the value that a homogenous subsurface would have given the same resistance values for the same electrode arrangement (M. Loke, 2011). To find the true resistivity of the subsurface, we need to invert the apparent resistivity using inversion software such as RES2DINV (M. Loke, 2011). During inversion, the best model that agrees with the measured apparent resistivity values, measured by the minimization of the root-mean square difference between the model and the data, is determined. Since different materials have different resistive characters, or transmit current differently, we can then interpret the inverted resistivity tomogram using geological knowledge to understand why there may be variations in resistivity. Kasprzak et al. (2017) compiled a range of resistivities in various geologic environments that can help discriminate between different waters and lithologies but lacks any discrimination between frozen sediments such as terrestrial permafrost and subsea permafrost (Figure 9).

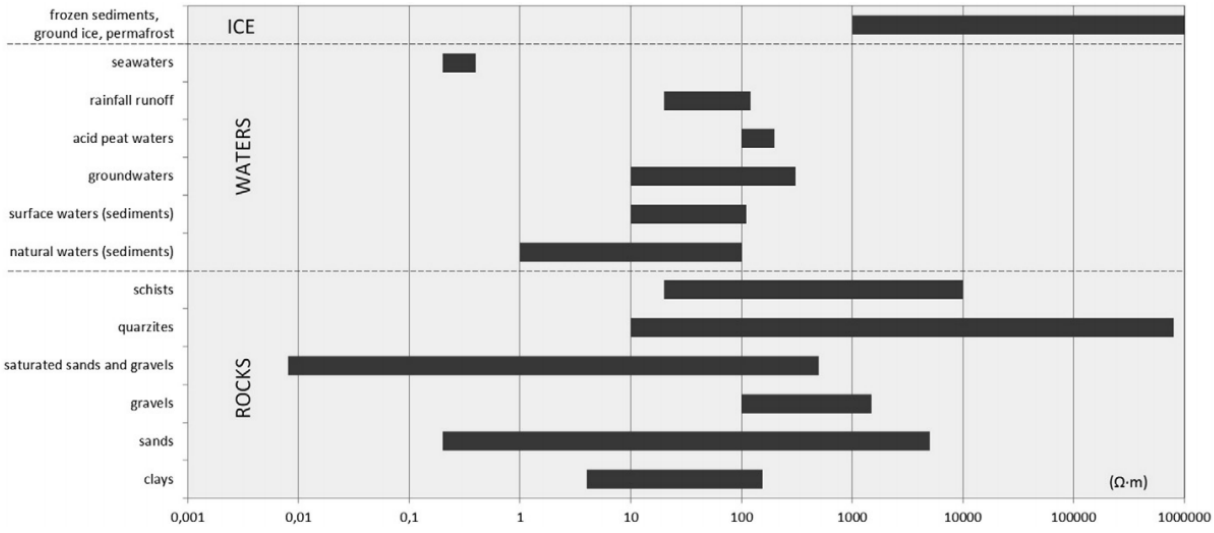

Figure 9: Resistivity ranges for typical Arctic materials (Kasprzak et al., 2017). Note that frozen sediments show up above 1000 Ωm.

Expanding on the scientific literature, we compiled additional previous studies focusing on ice-bearing permafrost, both in land and underwater, using different ERI arrangements to understand what ER values are most common for permafrost environments (Figure 10). Ice-bonded subsea permafrost usually manifests with an ER >10 Ωm or more in processed images of data from ER surveys towing floating electrodes behind a boat (so-called marine ER) while for ER surveys where electrodes are affixed to the ground, it usually manifests as >32 Ωm in underwater ER surveys and >1,000 Ωm in land surveys focusing on terrestrial permafrost (Figure 10).

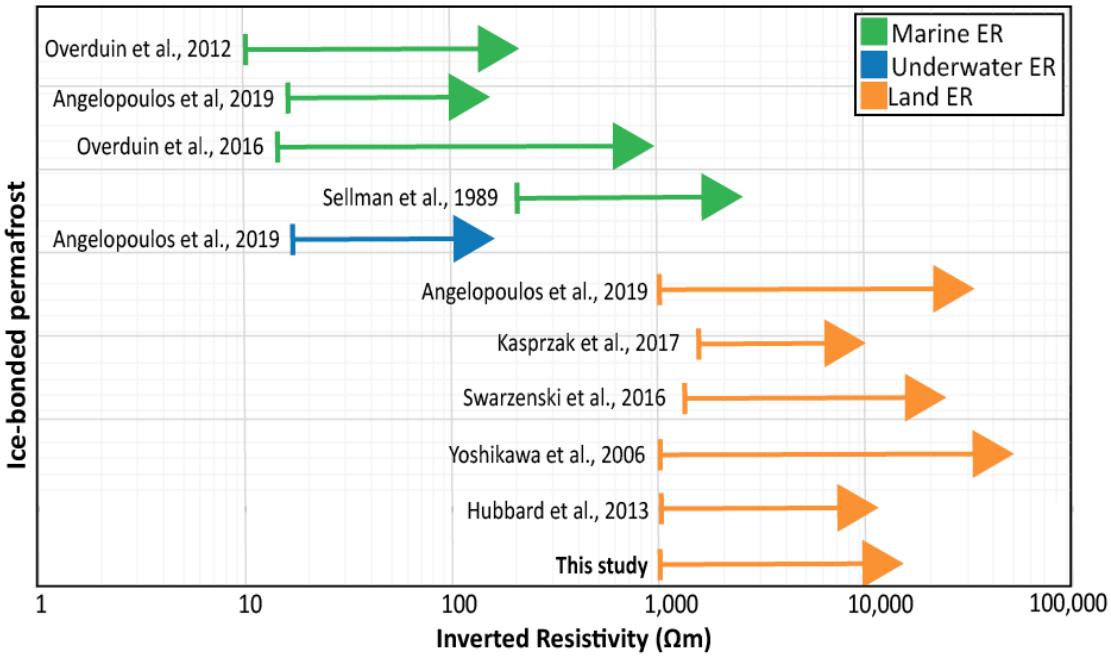

Figure 10: Synthesis of electrical resistivity values for ice-bonded permafrost. The values are synthesized from the literature with the context denoted by different colors (Angelopoulos et al., 2019; Hubbard et al., 2013; Kasprzak et al., 2017; Overduin et al., 2012; Overduin et al., 2016; Sellmann, Delaney, & Arcone, 1989; Swarzenski et al., 2016; K. Yoshikawa et al., 2006).

Taking advantage of the electrical properties of ice and saturated frozen materials, previous ERI applications in open coastlines of the Laptev Sea and Beaufort Sea as well as in the sheltered Elson lagoon in the Beaufort Sea revealed near-shore shallow subsea frozen permafrost continuously connected with terrestrial permafrost and sloping to greater depths offshore (Angelopoulos et al., 2019; Overduin et al., 2012; Overduin et al., 2016; Sellmann et al., 1989; Shakhova et al., 2017). Such scenario implies no hydrologic connectivity exists

between the onshore subsurface and the offshore subsurface other than through the active layer onshore and thin beach sediment layer (Figure 11).

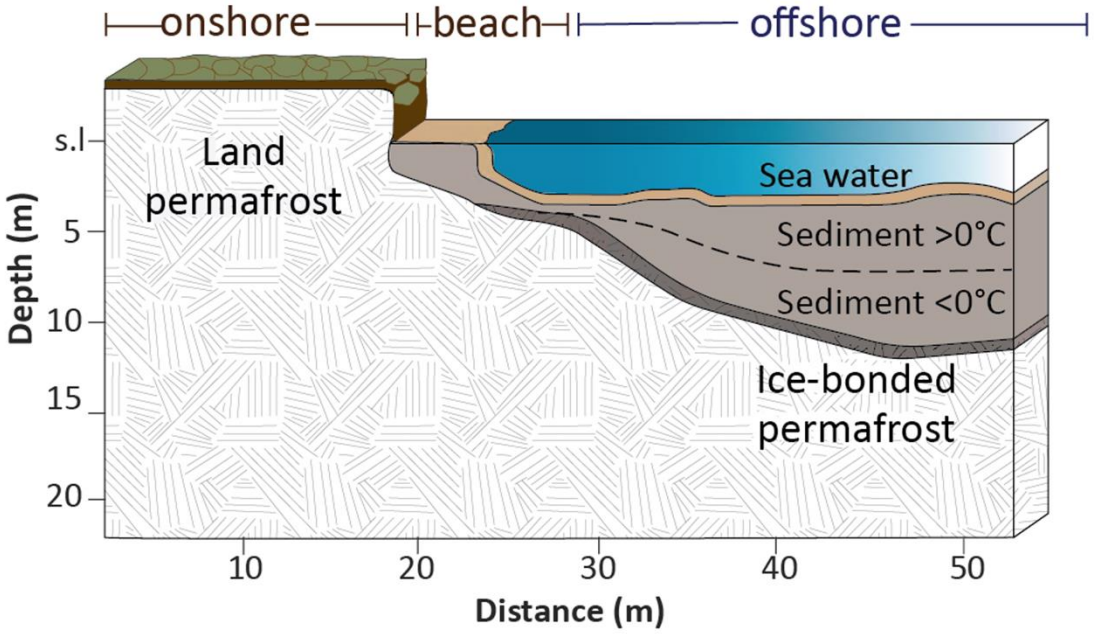

Figure 11: Near-shore subsea frozen permafrost continuously connected with land permafrost. Note that subsea permafrost is sloping to greater depths offshore.

Following the few existing coastal subsea permafrost investigations in the Beaufort Sea, we determined the subsurface resistivity distribution of an Arctic coastal lagoon to identify the presence and extent of frozen materials, freshwater and saltwater. Arctic sediments that were inundated by salt water during the LGM also exhibit higher pore water salinity. This must also be taken into account in the analysis and interpretation of any electrical resistivity survey results. Scientists have recovered soil samples from Arctic environments and measured the

electrical resistivity signal for varying temperature regimes. They observed that sediments saturated with salt-water freeze at lower temperatures than those saturated with fresh-water (0°C). A compilation of these laboratory measurements from different sources show that a typically increasing clay content and porewater salinity lowers the sample's freezing point, also known as freezing point depression (Figure 12). We will refer to this high-salinity and unfrozen sediment as cryopeg, as they are conventionally called in the permafrost literature. ERI can inform us on lithology, pore-water salinity and ice saturation, but it does not provide insights on the sediment temperature or location of the permafrost table (0°C isotherm), since not all sediment freezes at the same temperature. Salt-water saturated and/or clay sediments can exist below 0°C and remain unfrozen. Permafrost, by definition, can exist both frozen and unfrozen, as long as it remains below 0°C for at least two consecutive years. In this study, we focus on ice-bonded or frozen permafrost.

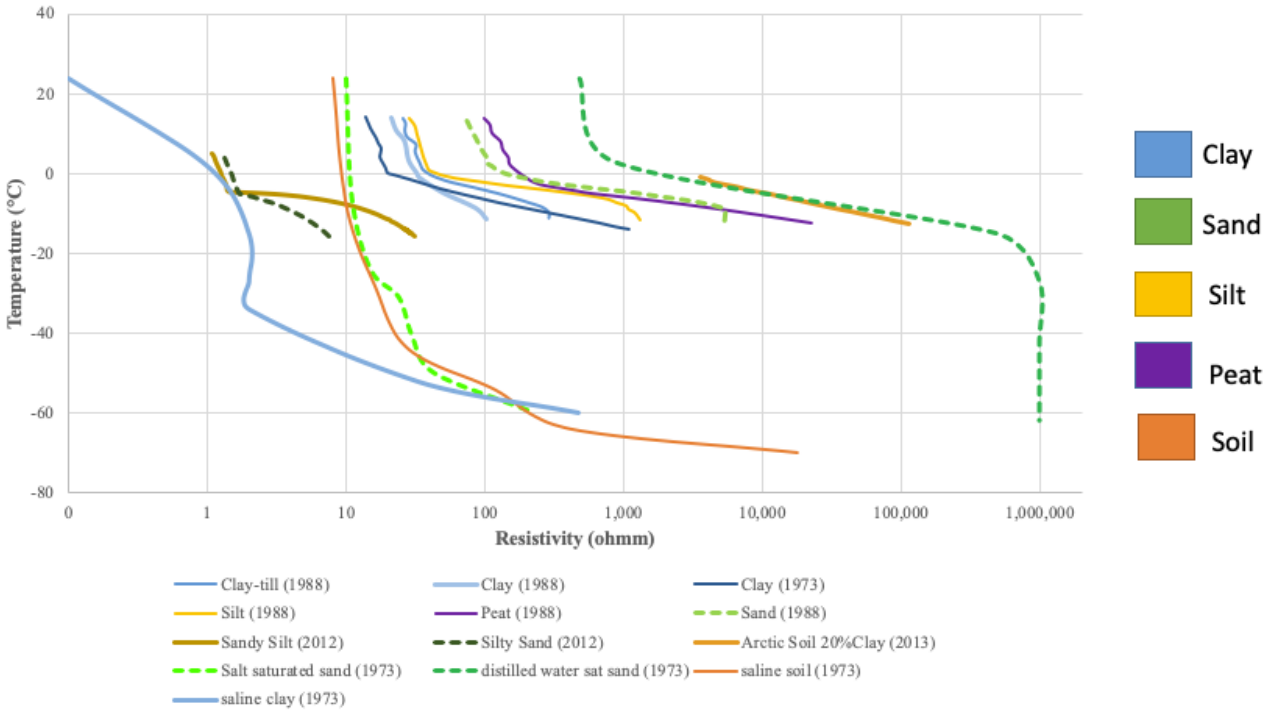

Figure 12: Sediment laboratory measurements of electrical resistivity at varying temperatures (Hoekstra, 1973; Olhoeft, 1975; W. Scott & Kay, 1988; W. J. Scott, Sellmann, & Hunter, 1978; Wu, Hubbard, Ulrich, & Wullschleger, 2013).

1.6 Research Goal & Objectives

The goal of this thesis is to advance understanding of the shallow subsurface across an exemplary Arctic coastal lagoon (Figure 13) using electrical geophysics. This goal is achieved by addressing the following specific research objectives.

Obj. 1. Identify the presence or absence of frozen subsurface materials.

Obj. 2. Evaluate the freshwater-saltwater dynamics in the near shore.

Obj. 3. Develop a comprehensive map of the lagoon subsurface.

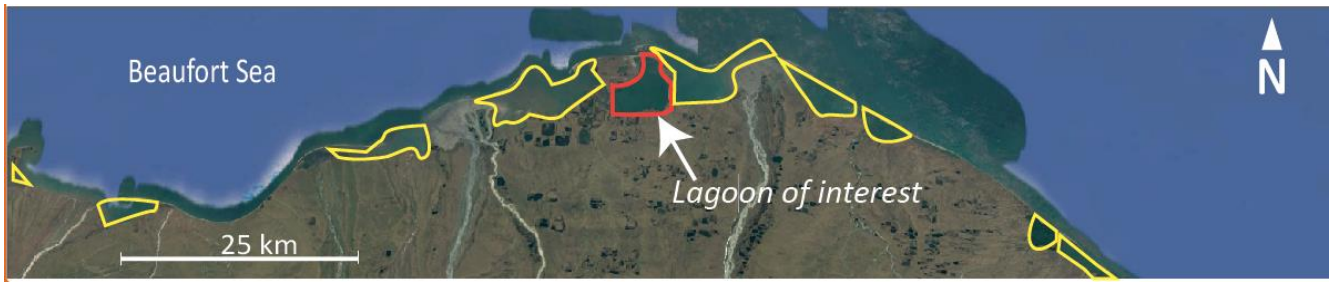

Figure 13: Kaktovik lagoon next to typical lagoons that line the Arctic coast.

1.7 RESEARCH APPROACH

This thesis presents the research in four main stages: (1) data acquisition, (2) data processing, (3) forward modeling, and (4) interpretation.

- We conducted ERI using a variety of survey configurations to develop a comprehensive map of the beach and lagoon subsurface. The surveys were done along the beach, across the beach and into the lagoon, and deep within the lagoon. All surveys were done in late summer (late July or August).
- We processed and inverted the acquired ERI surveys using the same inversion parameters.
- We conducted forward modeling to understand what 'apparent' resistivity should be expected for subsea permafrost underneath the lagoon by changing different parameters and if the geophysical method would detect the difference between a patch of permafrost on land and vertically continuous permafrost. In the forward modeling, we varied the following:

  1. Sea layer resistivity

2. Subsea ice-bonded permafrost resistivity
3. Land ice-bonded permafrost thickness
4. Using the forward modeling and geological knowledge as a backbone to our interpretations, we interpreted the ERI tomograms.

Chapter 2: Methods

We acquired ER surveys to detect the boundary of the ice-bonded permafrost within the sediment profile given the expected contrast of conductive ice-free and resistive ice-bonded sediment. ER measurements were acquired using three different field survey configurations:

- marine ER where floating electrodes are towed behind a boat,
- underwater ER where the electrodes are fixed to the sediment-water interface and,
- land ER where the electrodes are buried in the ground.

The ER surveys were acquired across the lagoon and at the coasts during the summers of 2014, 2015, and 2019 (Figure 14). We integrated the geo-electric observations with temperature observations, bathymetric measurements, water resistivity measurements, sediment samples and permafrost probing along the coast to provide hydrogeological context for our ER interpretations and to constrain the ER inversions.

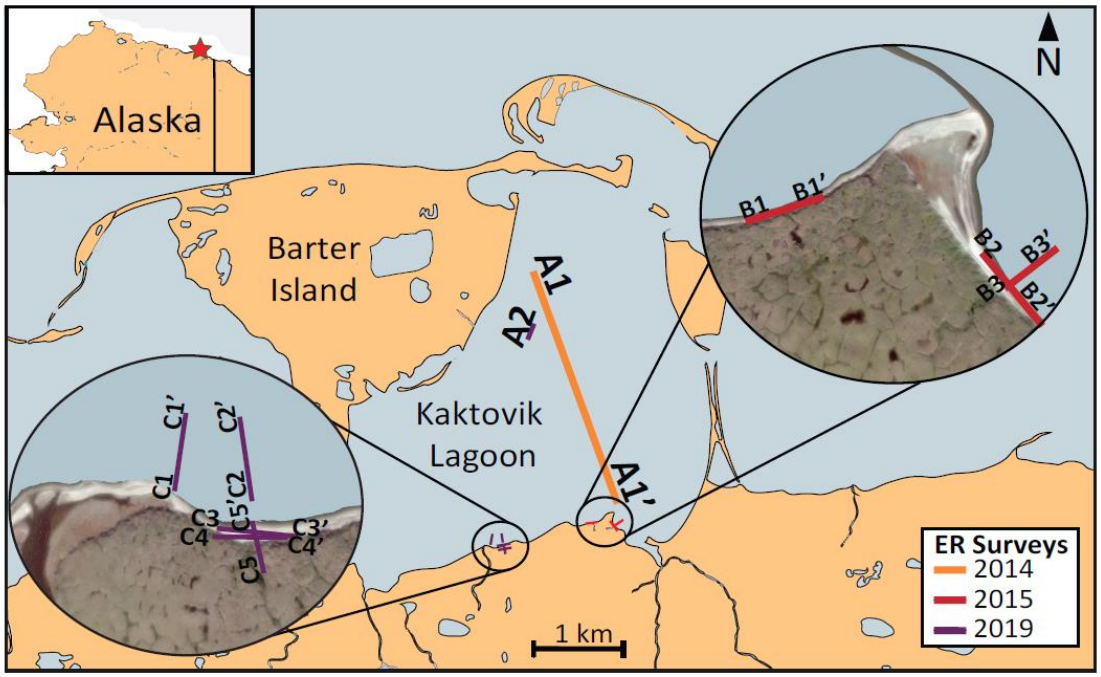

Figure 14: ERI surveys acquired across the lagoon and on the coast during summers of 2014, 2015, and 2019.

2.1 FIELD WORK

2.1.1 Marine ER Measurements

In August 2014, we used a SuperSting R8 eight-channel ERI system from Advanced Geosciences, Inc. to acquire approximately 4 km of marine ERI data (Figure 14, transect A1). We used a dipole-dipole array with floating electrodes towed behind a small boat (Figure 15). The potential electrodes were non-corrosive passive graphite electrodes 7 cm in length and 2.5 cm in diameter. The injection electrodes were stainless steel tubes of ~ 25 cm length and 5 cm

diameter. Electrode spacing was 3 m along the streamer and voltage was measured using 10 pairings of electrodes. Electrode position was determined using a marine GPS onboard, water depth was measured using an echo sounder attached to the boat, the injection current was measured, and the electrode pair potentials were recorded continuously at intervals of at least 1 m as the array was towed. At the same time as the marine ERI survey, the water layer resistivity was measured in the beach to be 0.27 Ωm using a handheld conductivity meter; this is similar to values reported in (Harris et al., 2017) for the center of Kaktovik Lagoon during August for the years 2011, 2012 and 2013, which averaged to 0.35 Ωm. This survey is referred to as 'marine ER'.

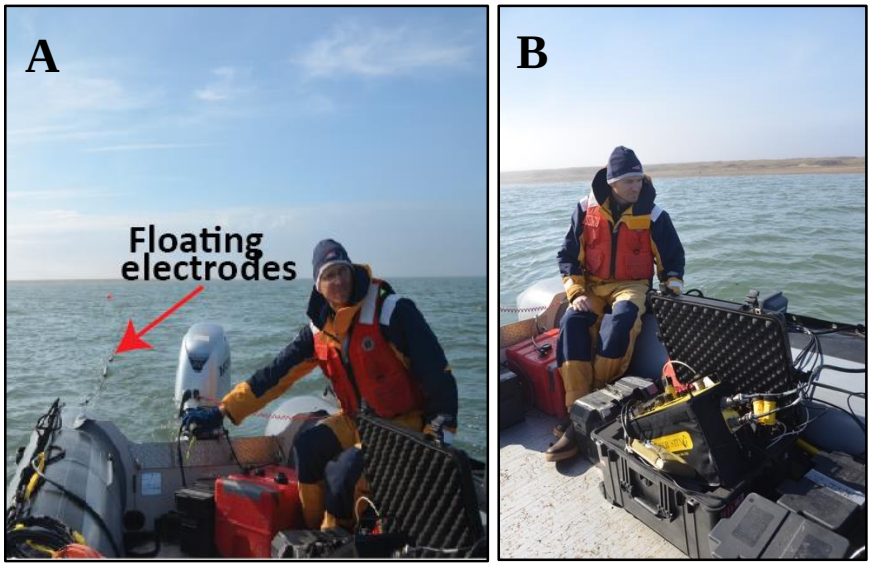

Figure 15: Marine ER survey. The boat is towing floating electrodes connected by a cable (A) and the ERI instrument brainbox powered by car batteries (B).

2.1.2 Terrestrial ER Measurements

A set of fixed electrode ERI surveys were conducted in August 2015 where electrodes were buried in the sediment in the southeastern field site (Figure 16 A). Two ERI surveys parallel to the beach shore were carried out using both a dipole-dipole array and a Schlumberger array with a 1.5 m spacing for a total length of 82.5 m. Both array types for each survey were merged together prior to inversion. In August 2019, two ERI surveys parallel to the beach shore and one orthogonal to the shore were carried out using the dipole-dipole electrode array with 1.5 m spacing in the southwestern field site (Figure 16 B). Topographic data was acquired using a portable laser theodolite to constrain the inversion. These are referred to as 'terrestrial ER'.

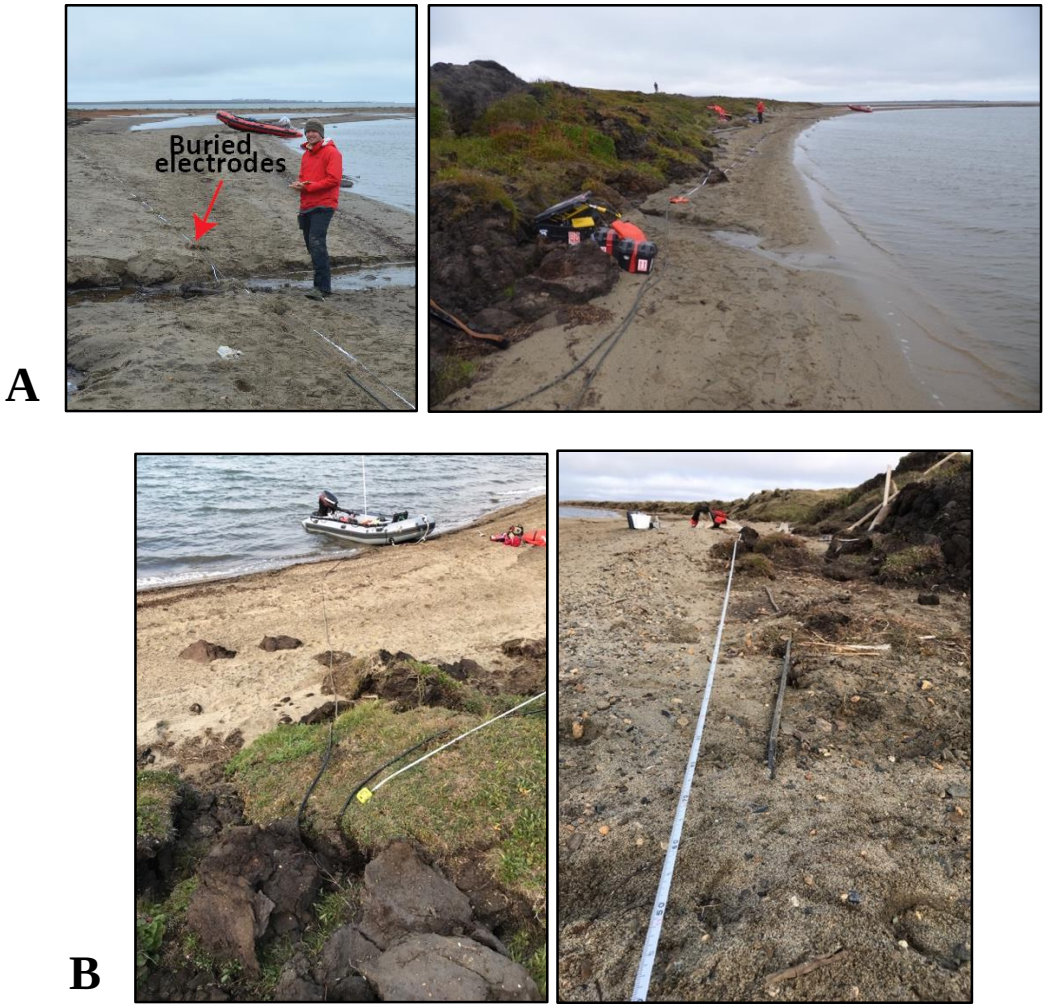

Figure 16: Terrestrial ER surveys. Electrodes are buried underneath the sediment to inject current into the ground in (A) 2015 and in (B) 2019.

2.1.3 Underwater ER Measurements

One underwater ERI survey was conducted perpendicular to the coast in 2015 and three in 2019 – these are referred to as 'underwater ERI' (Figure 17).

The electrodes were set on the seabed using lead weights and only observations

from the submerged electrodes fixed on the sea bed were analyzed. The dipole-dipole and Schlumberger surveys from 2015 were combined into one dataset prior to inversion. The sea layer resistivity was determined to be 0.25 Ωm using a handheld fluid electrical conductivity probe and the topographic data was acquired using a portable laser theodolite. On a few occasions, we directly probed for the frost table within the underwater ER transects using a 12-foot long folding aluminum rod (an avalanche probe) but did not encounter any hard materials.

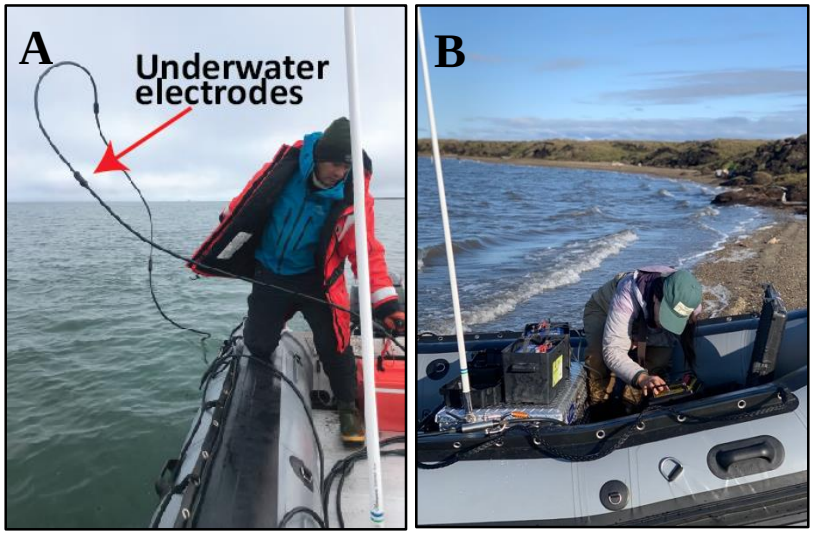

Figure 17: Underwater ER surveys. Electrodes are forced to sink onto the sediment-water interface by attaching weights onto the cable and allowing the electrodes to sink (A) and configuring the brainbox to run the surveys (B).

A combination of different ER configurations was used in this study and can be seen in Figure 18 below.

Figure 18: Photographs of the study sites and surveys. (A) is a picture of the southwestern site. The C transects (see Figure 14) are denoted by dashed lines in (A). (B) is a picture of the southeastern site looking west; it shows the B2 transect (see Figure 14). (C) is a picture taken during the boat-towed marine electrical resistivity survey within Kaktovik Lagoon (transect A1, see Figure 14). The end of the electrode streamer is marked by the red buoy in the picture in (C).

2.1.4 Salinity Measurements along the ER Lines

For one of the terrestrial ERI survey lines (Figure 14; transect C3), six holes roughly 50 cm deep were dug at different intervals along the line to

investigate if the pore water resistivity correlated with shallow sediment resistivity. Sediment porewater was allowed to fill in the hole before testing for its resistivity using a handheld fluid electrical conductivity probe (Figure 19).

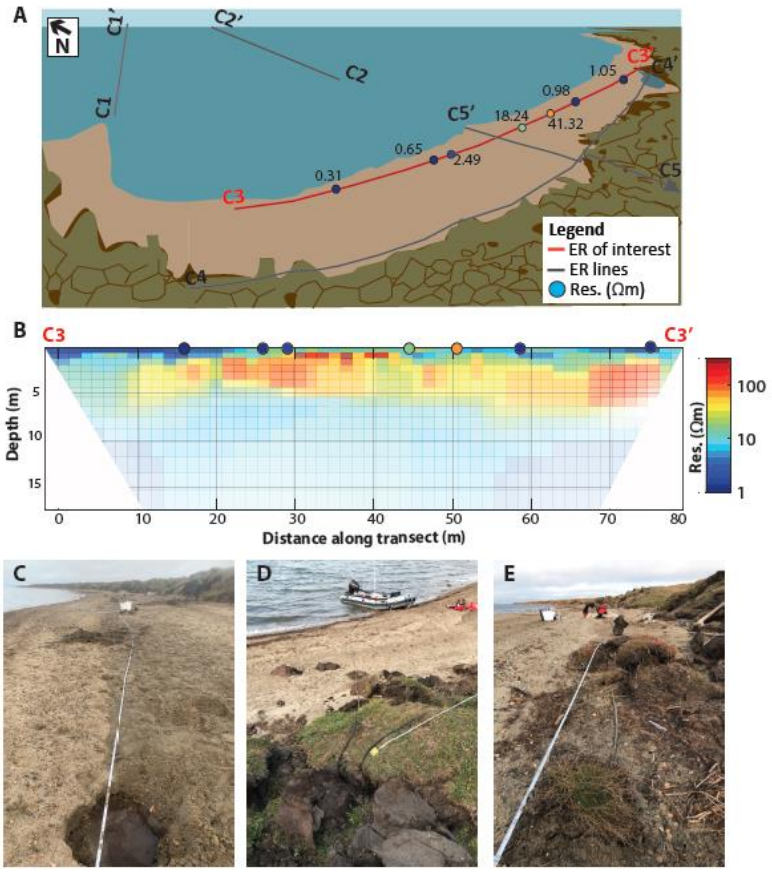

Figure 19: Comparison of surface borehole fluid ER with the tomogram for transect C3 and pictures of the transect. The ER of water from hand-dug surficial boreholes were measured with a handheld electrical conductivity meter. (C) shows the first hole along transect C3. (D) shows the first electrode of transect C4 while (E) shows the rest of C4. All pictures are facing east.

2.1.5 Sediment Samples

We verified that the sediment beneath the lagoon in the southwestern coast site (2019) was made up of coarse sand and gravel for the top ~50 cm of the sediment water interface (Figure 20).

Figure 20: Sediment samples. (A) Taken nearshore in 2019 at the sediment-water interface showing coarse sand and gravel and (B) a core from Kaktovik lagoon taken 100m from the shore in 2015 also showing a gravel top and sandy sediment for the first 50 cm.

2.1.6 Permafrost Probing

At the southwestern location, where transects C are located, we used a 120 cm long iron rod to probe for permafrost in the beach. This was qualitatively observed by reaching a depth where one could no longer push the rod through the sediment, indicating that we had hit ice. We were able to hit the ice at a depth of

18 cm on the tundra but the ice depth kept increasing as we moved towards the shore, shown by the plot in Figure 21 below.

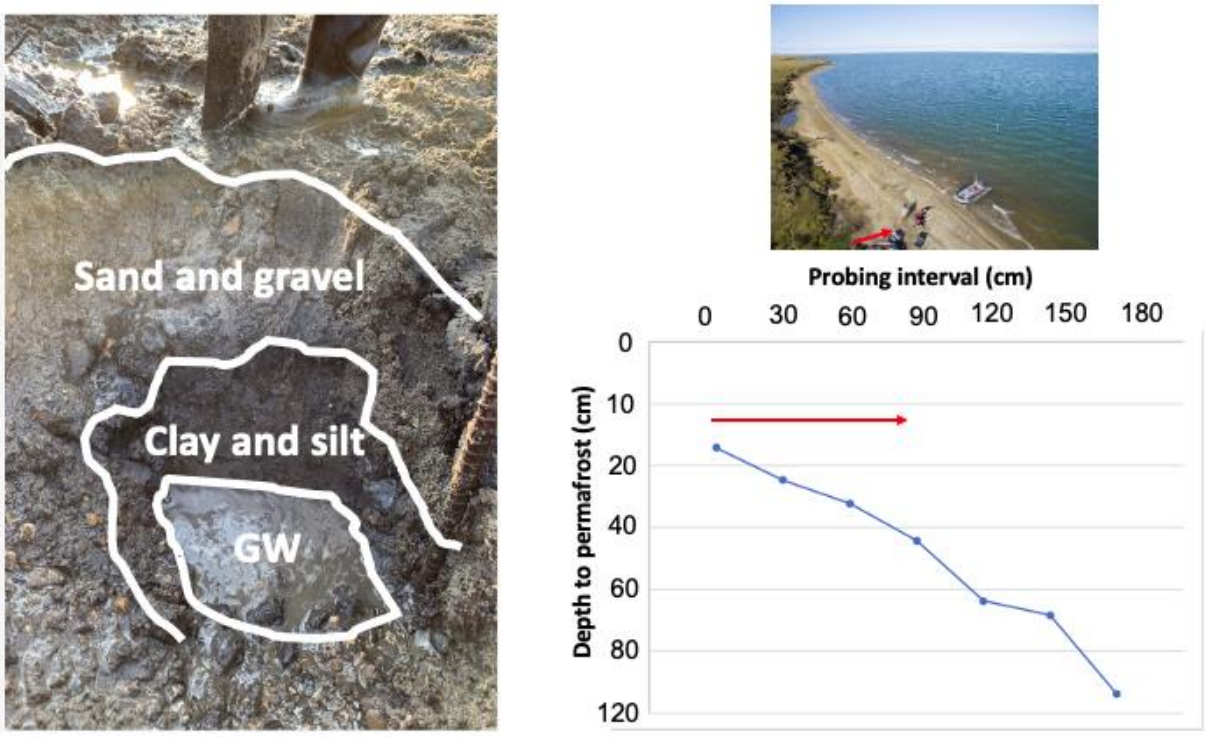

Figure 21: Permafrost probing. At southwestern location, we used a 120-cm-long rod to probe for permafrost from tundra towards the beach.

2.1.7 Ice wedges in Barter Island

We found massive ice present in the northern area of Barter Island facing Beaufort Sea (Figure 22). The bluffs were much greater in height than in our coastal study site areas and there was almost no beach. We present this as an example of a cross-section beneath the tundra where ice is present a few decimeters below the tundra.

Figure 22: Ice wedge in Barter Island. Massive frozen sediment in Northern Barter Island below a 70 cm insulating active layer.

2.2 Data Processing and Inversion

2.2.1 Inversion of ER Survey Data

All underwater and terrestrial inversions were implemented using the software RES2DINV to invert the apparent resistivity data using a robust data constraint L1 Norm inversion method (M. H. Loke & Barker, 1996). The data from the marine ERI was inverted using AGI Earth Imager 2D software with the same inversion settings. Inversion performance was indicated by the root mean square (RMS) error between the field apparent resistivity measurements and the apparent resistivity data calculated from the inverted model. Inversion continued until the RMS error between subsequent iterations was <5%, usually between 3-7 iterations. The sea layer resistivity was fixed for the marine and underwater ERI surveys based on field data. The inversion parameters can be found in Table 1.

Table 1: Resistivity inversion parameters. Inversion parameters implemented in RES2DINV.

Inversion Parameter	Setting
Numerical model	Finite-element
Inversion Method	Robust inversion (L1 Norm)
Robust data cut-off factor	0.05
Nodes	4
Damping	0.01
V/H filter	0.5
Model discretization	Blocks have same width
Model discretization	Reduced effect of side blocks
Mesh parameters	Finest mesh grid size
Limit resistivities	None
Iterations	<7
RMS	< 5%

2.2.2 ER Model Resolution

In order to quantify how well ER is able to resolve a feature at a given depth, we quantified the model "resolution" values following the model resolution equation that relates the calculated model resistivity, q_{Model}, to the field resistivity, q_{True} (Day-Lewis, Singha, & Binley, 2005). This essentially treats the resolution

matrix, R, as a filter through which the inversion method attempts to resolve the subsurface resistivity. R is defined as:

$$R = q_{Model} / q_{True}$$ **Equation 1:** Resolution Matrix.

In general, the resolution is greatest near the surface where the electrodes are placed and rapidly decreases with depth. We used the resolution matrix to control the transparency of the data blocks making the lower resolution values more transparent and the higher resolution values more opaque. In addition, we applied an edge filter where with a slope of 1:1 to blank out data in the edges where current is less likely to penetrate and thus where data is unreliable.

CHAPTER 3: Forward Modeling

In this chapter, we present synthetic geophysical models based on geologic information to evaluate the feasibility of the ERI method in detecting permafrost beneath the sea bed using field survey configurations. The goal is to use these synthetic model results as the basis of our interpretations to determine if ice-bonded permafrost was or can be detected beneath the lagoon. This chapter will describe the forward modeling done to better understand:

- Marine ER sensitivity analysis to sea water and ice-bonded permafrost resistivity changes.
- Terrestrial ER sensitivity analysis to land ice-bonded permafrost thickness.

3.1 Forward Modeling of Marine ER Surveys

Before processing and interpreting the ERI data, modeling of theoretical scenarios was carried out using the forward modeling software RES2DMOD by Geotomo Corporation where we evaluated the effects of different stratigraphic layering patterns, permafrost resistivities and land permafrost thickness. For construction of synthetic marine ER models, we used the known lagoon average water depth and the survey design used for the marine ERI survey. That is, the prescribed theoretical (and true) resistivity field was sampled following the design of a field survey. The resultant data from this synthetic field survey was then

analyzed as if it were field data and subsequently inverted. The inversion settings for the synthetic model data are exactly the same as the settings used for inverting the real field data.

We first considered two sets of synthetic marine ERI scenarios:

- To simulate the effect that a salty or fresh water layer would have on the resistivity at which permafrost is detected using the field survey configurations, the water layer was varied in the model.
- To determine the minimum and maximum value of resistivity at which ice-bonded permafrost would be detected at, the water layer was kept constant resistivity but the resistivity of ice-bonded permafrost was varied.

To explore the different scenarios, a three layered petro-physical model was constructed. The model had a 3.5 m thick sea layer, a 1.5 m thick thawed saturated sediment layer and a 5 m thick ice-bonded permafrost layer in the bottom (Figure 23). To represent realistic field conditions, 3% noise was added to

the apparent resistivity (the resistivity 'measured' by the synthetic sampling) prior to inversion.

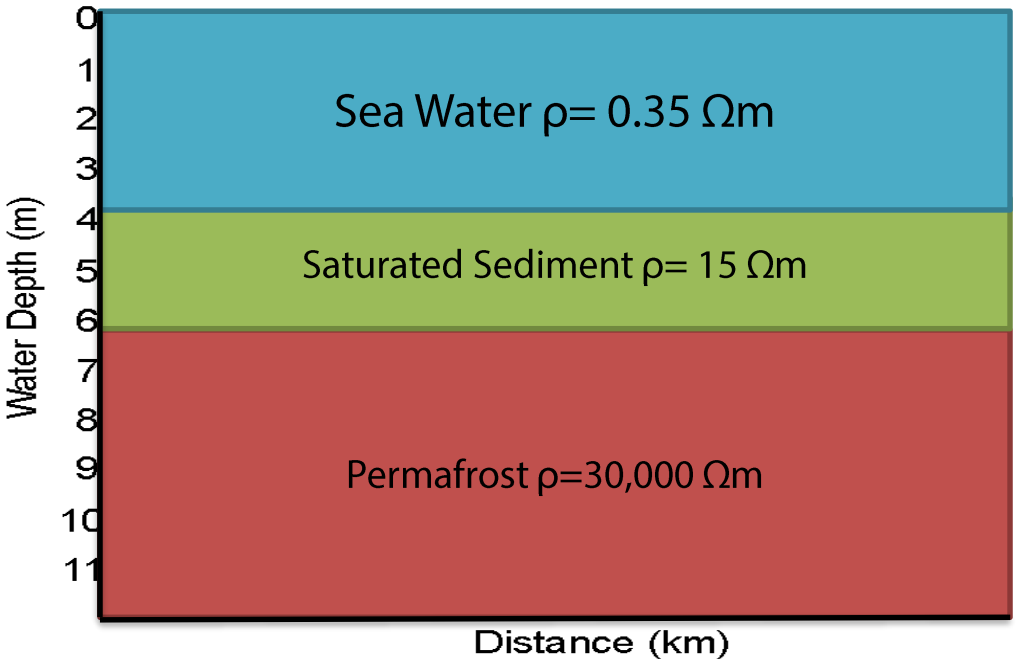

Figure 23: Forward model for marine ER survey. There are three layers: 4 m deep lagoon water at 0.35 Ωm, a 2m thick saturated sediment of 15 Ωm and a permafrost resistivity of 30,000 Ωm.

The ice-bonded permafrost resistivity was constrained for the first set of scenarios and the sea layer resistivity was constrained with average overall salinity values from Harris et al.'s (2017) lagoon salinity monitoring results for the second set of scenarios. However, to calculate the value for the saturated sediment layer, we used Archie's law.

$$\rho_b = a\phi^{-m}S_w^{-n}\rho_w$$ **Equation 2:** Archie's law.

We assumed tortuosity a=1 (D. Jackson, Taylor Smith, & N. Stanford, 1978), porosity ϕ=35% (typical for gravel and sands), fully saturated marine sediment with saturation ratio S_w=1, and fluid resistivity of ρ_w=0.35 Ωm when considering sea water-saturated sediment and ρ_w=15 Ωm when the fluid is freshwater (Table 1). The cementation factor (m) was set to 1.983 (Pearson et al., 1983).

Other scientists have found that thawed sediment samples below the seabed have ER that ranges between 10 and 30 Ωm in the Beaufort Sea; this lies within the ranges of sea water saturated (3 Ωm) and freshwater saturated (122 Ωm) thawed sediment values calculated in Table 2 (Overduin et al., 2012). Thus, a 15 Ωm value was chosen to be representative of the saturated thawed sediment layer between the water layer and permafrost.

Table 2: Saturated sediment estimation using Archie's law.

		Seawater Saturated	Freshwater Saturated
ρ_b	Bulk Resistivity	3	122
a	Tortuosity Factor	1	1
ϕ	Porosity	0.35	0.35
m	Cementation Factor	2	2
S_w	Saturation	1	1
n	Saturation Exponent	2	2
ρ_w	Fluid Resistivity	0.4	15

Previous ERI tomograms show that ice and permafrost ER values in inverted data vary greatly from glacial ice (10^8 Ωm) to low saturation ice-bonded saline permafrost (10^2 Ωm). The individual ranges for terrestrial and marine permafrost are narrower however, suggesting that current channeling may

significantly impact the resistivity signal of permafrost beneath a conductive sea layer.

To investigate the effect that a salty or fresh water column would has on the resistivity at which underlying permafrost is detected using the survey configurations, the sea layer resistivity was varied in the models while permafrost and the saturated sediment layers were kept at constant resistivity (Figure 24). The water layer resistivity was varied from 0.1 to 8 Ωm.

The results of the synthetic modeling facilitate the understanding of the most important theoretical factors to take into account when conducting a marine ERI survey and is critical to the interpretation of the ERI field data acquired in Kaktovik Lagoon.

Permafrost with an actual and prescribed ρ value of 30,000 Ωm appears in the inverted tomogram as a layer with a ER below 100 Ωm and above 10 Ωm for imposed water column resistivities <1 Ωm (Figure 24) which is an apparent limit for seawater and above the range observed in Kaktovik Lagoon.

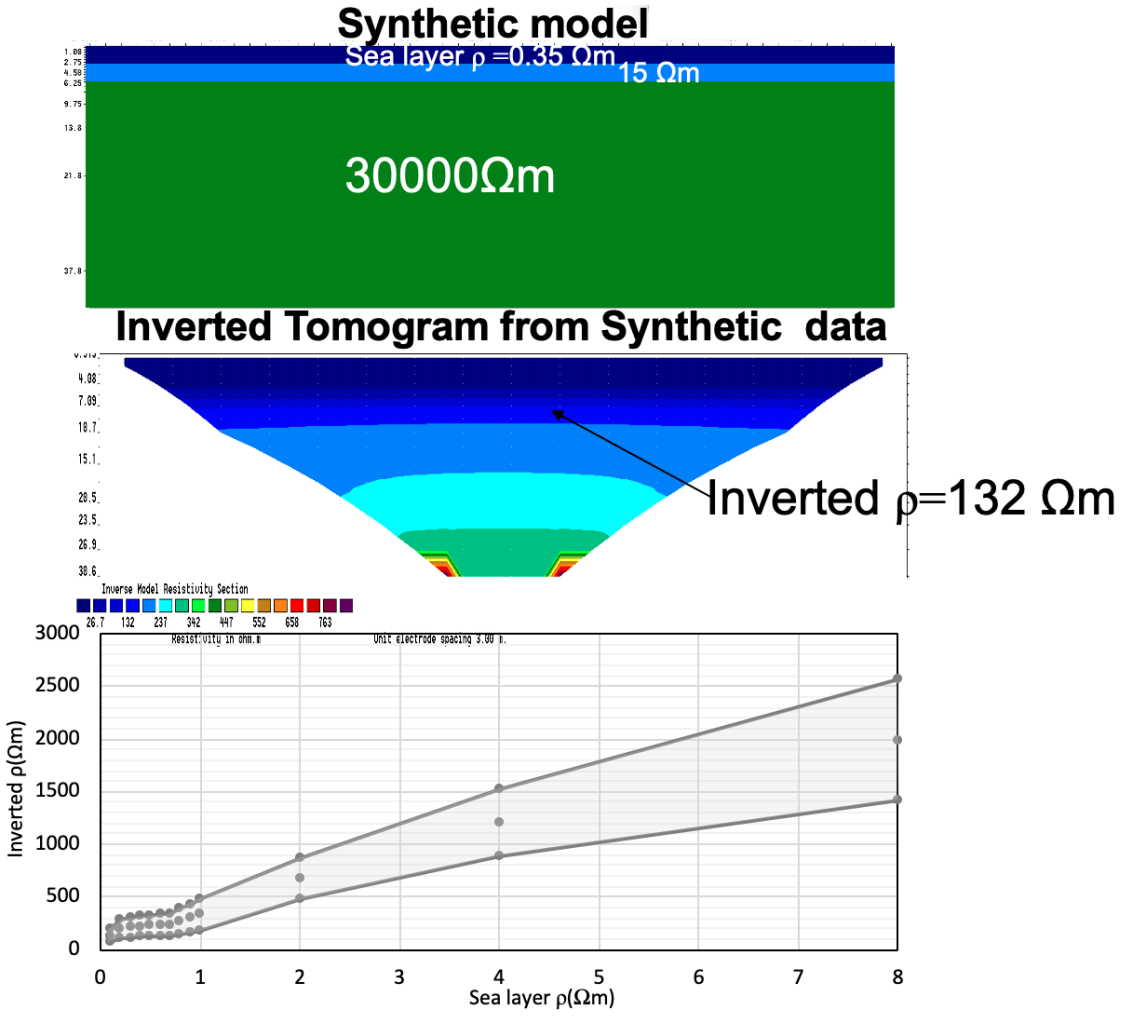

Figure 24: Water layer resistivity is varied. Water layer varies from 0.1 to 8 Ωm and the value for the inverted resistivity value for permafrost is recorded.

The much lower inverted ER compared to the actual prescribed ER highlights that current channeling is occurring where the resistive signal of permafrost is blurred and diffused by several orders of magnitude by the presence of a very conductive overlying sea layer. As the water layer becomes fresher and thus increasingly resistive, so does the inverted ER of permafrost. This implies that one cannot use the ER value obtained for subsea permafrost from tomograms to calculate other properties using petro-physical relationships. Furthermore, marine ERI is more effective when used in freshwater rather than salty water. It is imperative to accurately know the sea layer ER for robust interpretation. Previous ERI studies of terrestrial ice-bonded permafrost where current channeling is less likely reported resistivity values between 1000-10,000 Ωm (Angelopoulos et al., 2019; Fortier, LeBlanc, Allard, Buteau, & Calmels, 2008; Olhoeft, 1975; Vanhala, Lintinen, & Ojala, 2009). Studies that used marine ERI in the coastal Arctic environment reported ρ for subsea ice-bonded permafrost between 10-100 Ωm (Angelopoulos et al., 2019; Overduin et al., 2012). Given the large variation of reported ER values for permafrost, the effects of actual permafrost ER was evaluated using a fixed water layer ER of 0.35 Ωm to determine the minimum and maximum resistivity at which permafrost would appear in inverted tomograms (Figure 25).

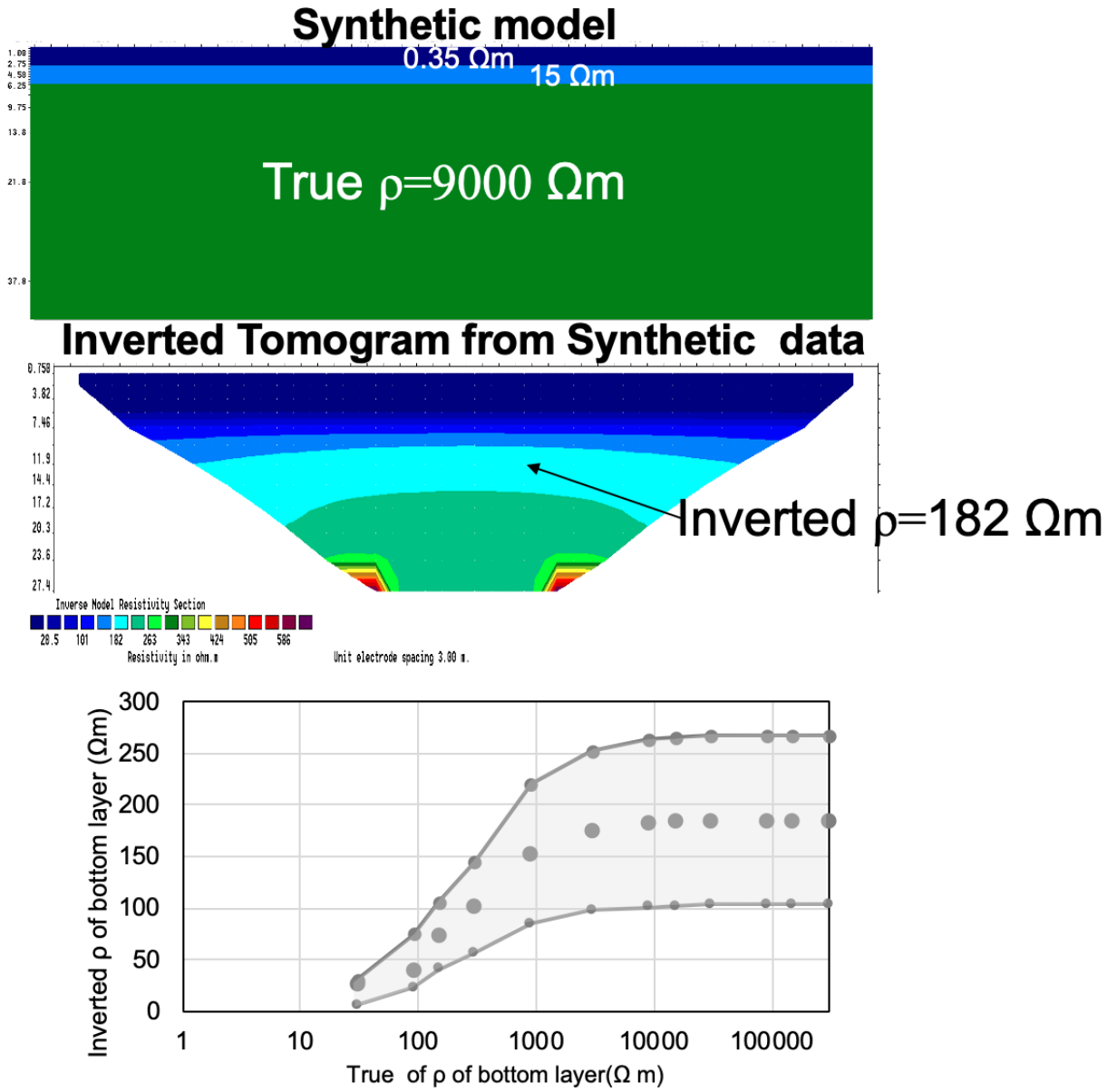

Figure 25: Permafrost resistivity is varied. It changed from 50 to 50,000 Ωm, we can observe that we detect it it's specific resistivity until 10,000 Ωm. Any changes above 10,000Ωm will be detected as a resistivity lower than 300 Ωm.

Permafrost with a ER value greater than 3,000 Ωm manifested as a zone with an ER between 250-300 Ωm (Figure 25). This second set of synthetic scenarios highlights that even though the sea layer ER is known (0.35 Ωm), and when subsea permafrost ER values range between 3,000 Ωm and 100,000 Ωm, it will manifest as values ranging between 250-300 Ωm in inverted tomograms for Marine ER (Figure 25). An asymptotic relationship exists between the true ER of permafrost and the ER which it is manifested in inverted tomograms when a conductive sea layer is present on top. Over-all submarine permafrost always manifests as having a ρ between 50-300 Ωm in the presence of a 3 m-thick conductive sea layer.

Using the forward modeling results as the backbone for our interpretation, we compared the results from the forward model to that of the acquired marine ER survey. After the marine ER transect A1 (Figure 14, transect A1) was acquired in August 2014, the data was inverted. We selected a 100 m section of the 4 km survey to further analyze and compare to the forward modeling results (Figure 26).

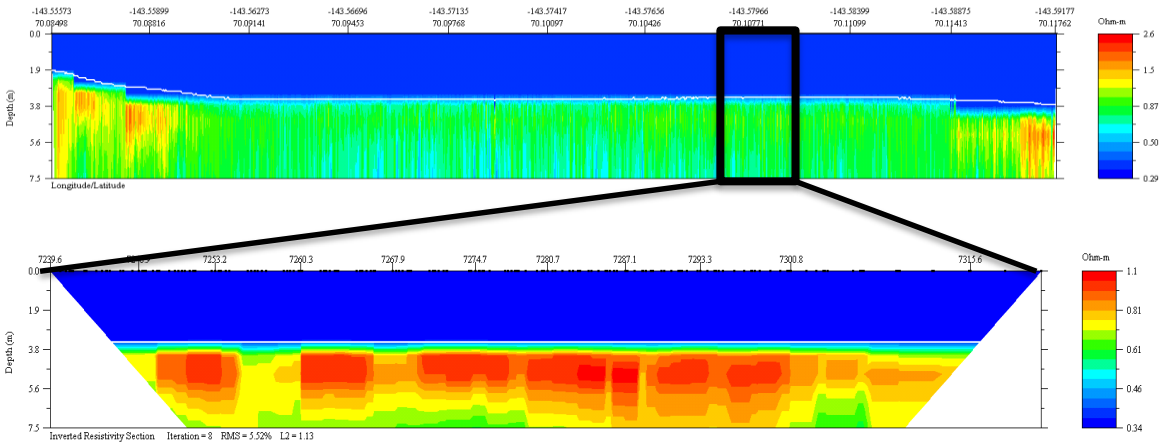

Figure 26: Trimmed inverted ER for transect A1. A section 100m that varies between 0.34 Ωm and 1.1 Ωm was randomly selected for further analysis.

The inverted ER survey indicated a mostly homogeneous two-layered earth with a conductive water layer fixed at 0.35 Ωm and a resistive bottom sediment layer. The bottom layer resistivity was varied in the model to evaluate which model scenario best fit the inverted field data (Figure 27).

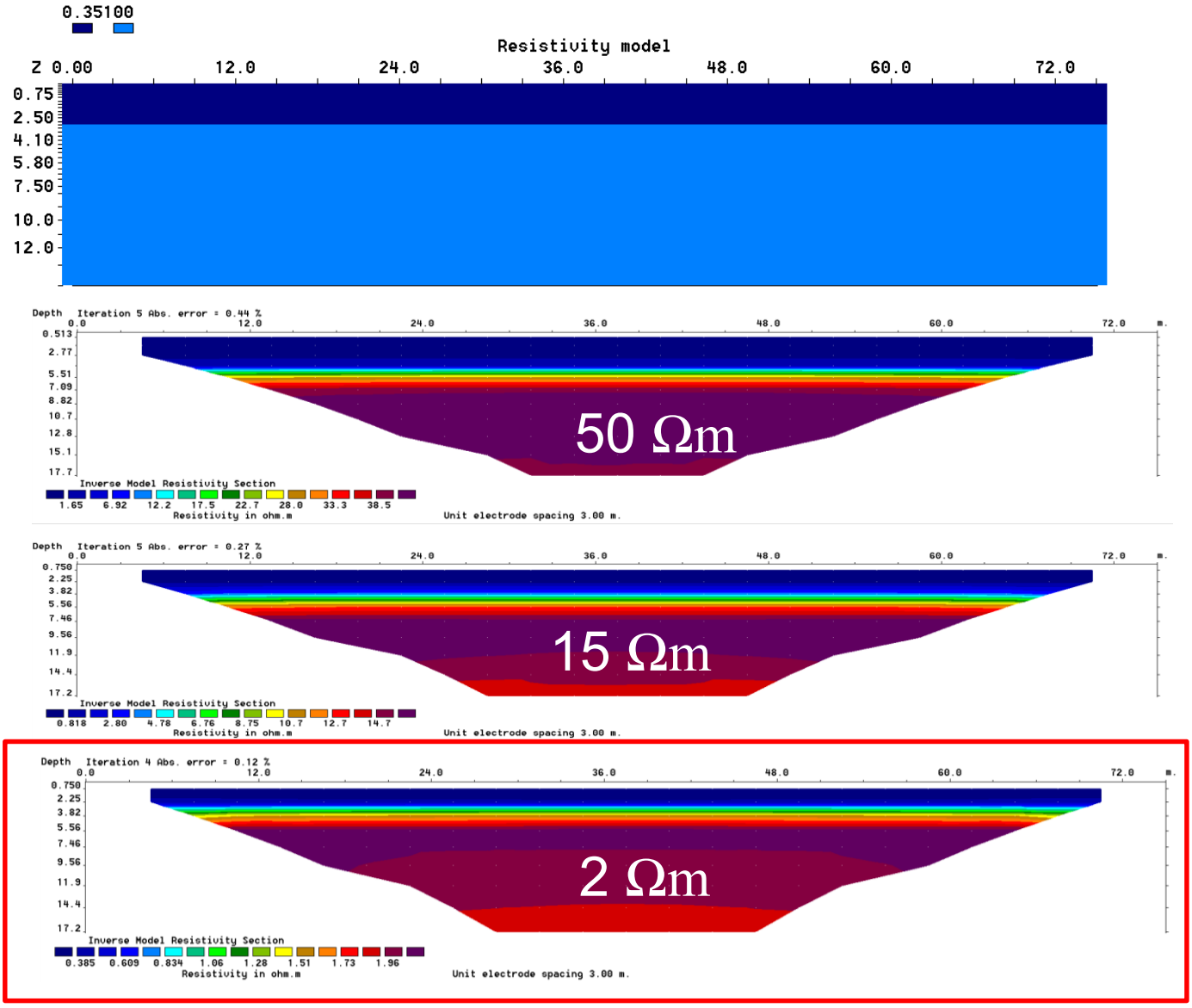

Figure 27: Forward modeling of a two layered system. Water layer is fixed at 0.35 Ωm and the homogeneous sediment indicates that the constrained resistivity used in the model.

The sediment layer with resistivity of 2 Ωm best matches the inverted field data which suggests that the resistive signal underneath the water layer is not that of ice but rather a lithological resistive signal.

In order to understand the resistivity variations that could occur due to a change in porosity and tortuosity. Tortuosity was calculated using Bruggeman's equation used for random packs of grains of porosity $\phi > 0.2$ (Bruggeman, 1935).

$$\tau = \phi^{1/2}$$ **Equation 3:** Bruggeman equation

Where τ denotes tortuosity and ϕ denotes porosity. Porosity was varied between the minimum value for porosity of sand/gravel (ϕ =0.25) and the maximum value for porosity of clay, ϕ =0.70 (Castro, Ballesteros, Méndez, & Tarquis, 2014).

The minimum and maximum resistivity values for the thawed sediment was determined using the minimum and maximum porosity and tortuosity values for both sea water saturated sediment (Table 3) and freshwater saturated sediment (Table 4).

For salt-water saturated sediment, the resistivity did not increase significantly (only 2 Ωm) with a decrease in porosity of 45% and a decrease of 30% of tortuosity (Table 3). However, for the fresh-water saturated sediment, there was an increase of 114 Ωm with a decrease in porosity of 45% and a decrease of 30% of tortuosity (Table 4). This indicates that the saline saturated

unfrozen substrate is not as sensitive to changes in porosity or tortuosity as fresh water saturated sediment.

Table 3: Salt-water saturated sediment resistivity estimation using Archie's law.

$\rho_b = a\phi^{-m}S_w{}^{-n}\rho_w$		Higher porosity	Lower porosity
ρ_b	Bulk Resistivity	1	3
a	Tortuosity Factor	0.8	0.5
ϕ	Porosity	0.70	0.25
m	Cementation Factor	2	2
S_w	Saturation	1	1
n	Saturation Exponent	2	2
ρ_w	Fluid Resistivity	0.4	0.4

Table 4: Freshwater sediment resistivity estimation using Archie's law.

$\rho_b = a\phi^{-m}S_w{}^{-n}\rho_w$		Higher porosity	Lower porosity
ρ_b	Bulk Resistivity	26	120
a	Tortuosity Factor	0.8	0.5
ϕ	Porosity	0.70	0.25
m	Cementation Factor	2	2
S_w	Saturation	1	1
n	Saturation Exponent	2	2
ρ_w	Fluid Resistivity	15.0	15.0

3.2 Forward Modeling of Land Ice-bonded Permafrost

On land, forward modeling was conducted in order to interpret transect C5 which started on the tundra, on top of an ice polygon, and ended at the beach shore. The forward modeling was conducted using RES2DMOD to determine if ER was a feasible method to detect ice-bonded permafrost depth on land since ice

does not allow current to be transmitted as easily and might create a current obstruction at depths. Two synthetic ER scenarios were constructed with three ER units representing ice-bonded permafrost (5,000 Ωm), unfrozen salt water-saturated or fine grain sediment (20 Ωm), and relatively fresh water-saturated or coarse grain sediment (200 Ωm).

- Shallow ice is present only in the top of the ice polygon.
- Ice extends deep into the subsurface.

The hypothetical ER scenarios were then synthetically surveyed following the same dipole-dipole design as the field surveys. The resulting synthetic survey data was inverted following the same protocol used for inverting the real field data using RES2DINV and compared to the actual field data, transect C5, without topography (Figure 28).

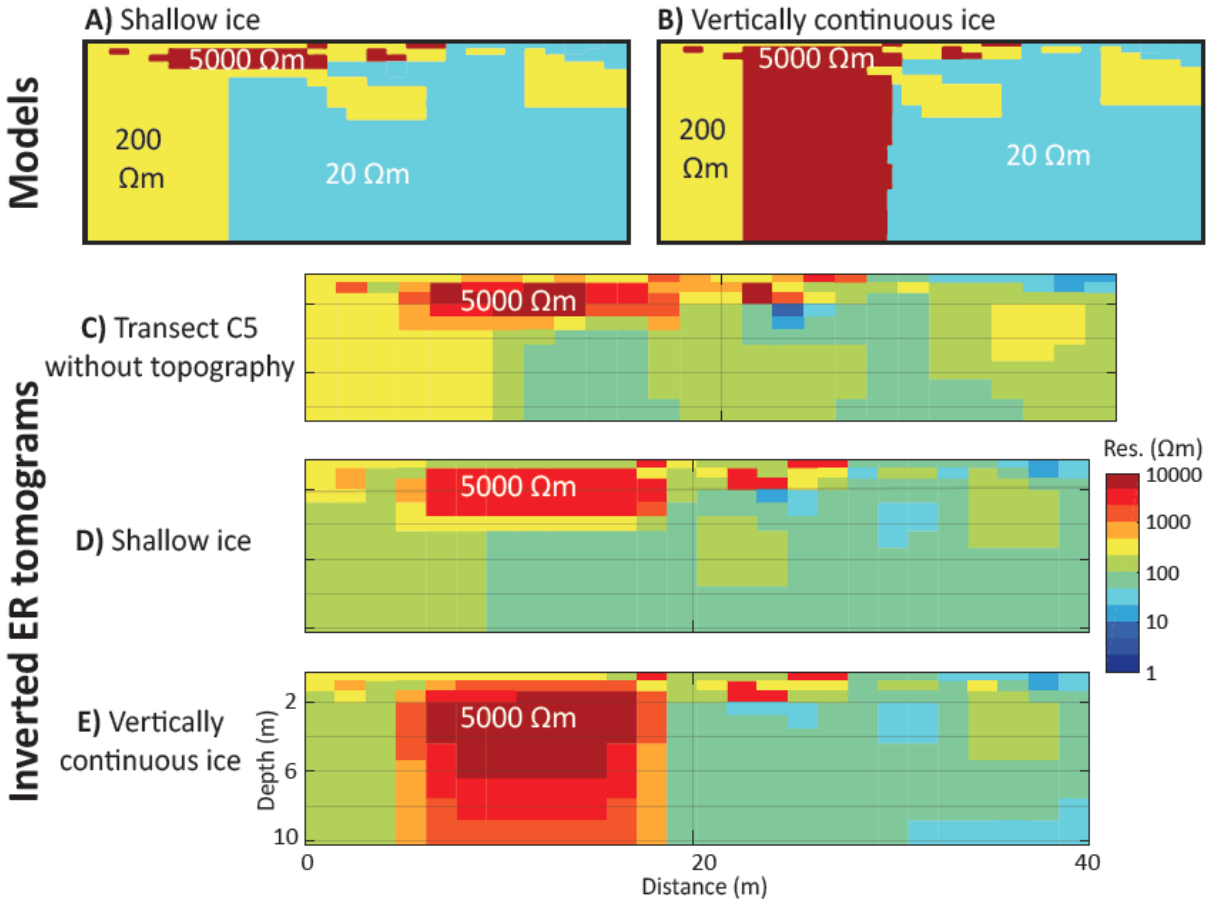

Figure 28: Land ER forward modeling design and results. The figure shows two synthetic forward models, i.e., hypothetical electrical resistivity (ER) fields with (A) shallow ice-bonded permafrost (5,000 Ωm) and (B) vertically continuous ice-bonded permafrost and their corresponding inverted ER tomograms (D and E).

The shallow ice tomogram and the tomogram for transect C5 (C) are similar, suggesting that the ice-bonded permafrost detected within C5 is of shallow extent and that the zone beneath is not frozen. This implies that ER is a feasible method to discriminate between ice thickness in land ice-bonded permafrost environments.

Chapter 4: Results

This chapter describes the electrical resistivity distributions in the subsurface of the lagoon and at the coasts. A total of ten apparent resistivity profiles were acquired consisting of:

- Five shallow and deep profiles within the lagoon: one marine ER and four underwater ER surveys.
- Five terrestrial ER surveys at the coast of the lagoon: one perpendicular to the beach and four parallel to the beach.

4.1. SHALLOW AND DEEP ELECTRICAL RESISTIVITY PROFILES WITHIN THE LAGOON

Marine ERI surveys using floating electrodes conducted in summer 2014 showed that electrical resistivity increased gradually from 0.35 Ωm in the water column to 1.6 Ωm within the lagoon sediment at the bottom of the profile. The most resistive areas around Kaktovik Lagoon were found close to the southwest shore (Figure 29; section A1). The vertical gradational pattern in resistivity is surprisingly uniform across the approximately 4 km-long transect (which crosses almost the entire lagoon), where the full extent of the profile reaches 7.5 m below the water surface and approximately 4 m below the sediment-water interface.

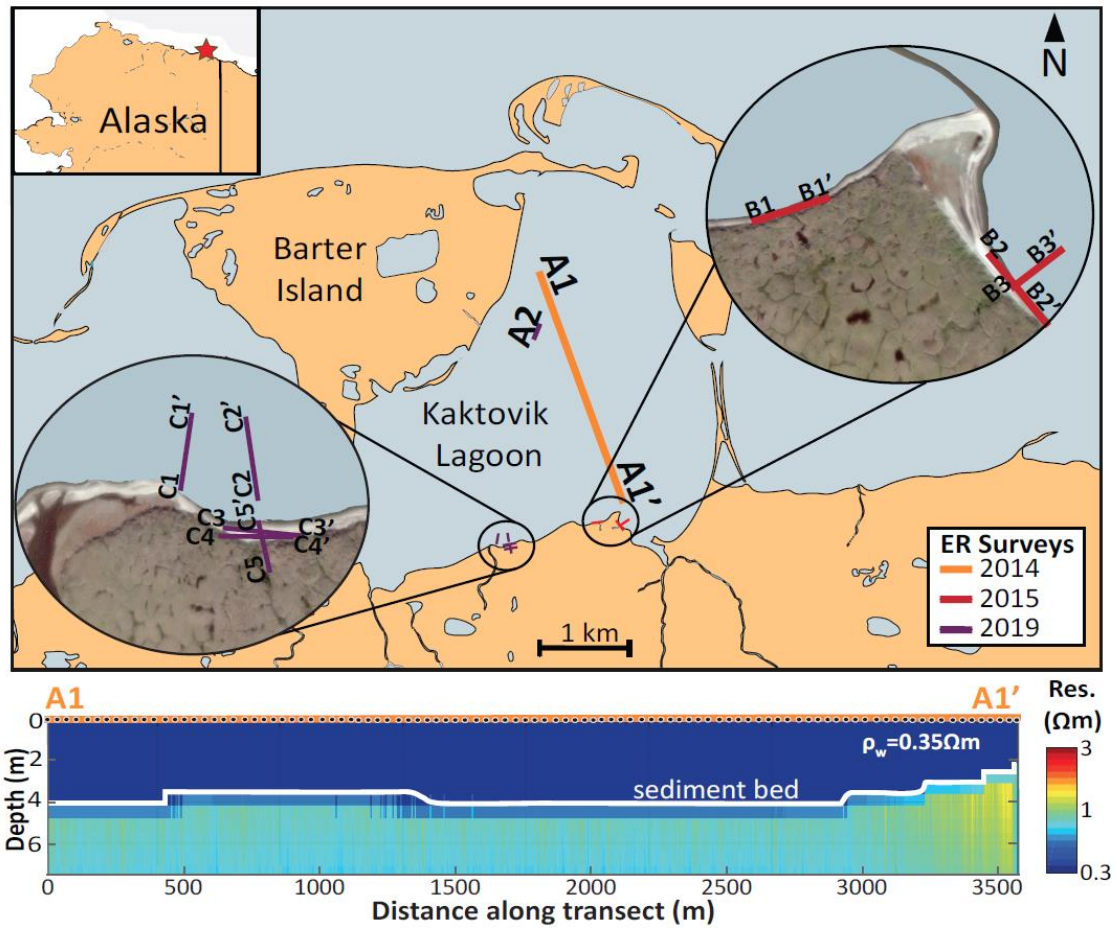

Figure 29: Overview of the study site and locations of electrical resistivity survey lines. The figure shows the location of Kaktovik Lagoon (inset) and the positions of a boat-towed marine ERI (A1) survey conducted in 2014, two terrestrial (B1 and B2) and one underwater (B3) ERI surveys conducted in 2015 and three terrestrial (C3, C4, and C5) and three underwater (A2, C1, and C2) ER surveys conducted in 2019. The bottom panel shows the inverted tomogram for survey transect A1-A1' with water layer fixed at 0.35 Ωm, bathymetry data (white line) and logarithmic color intervals.

To extend the results from summer 2014 for depths greater than 4 m below the sediment, we conducted an underwater survey in 2019 where electrodes were placed on the water-sediment interface which imaged down to 17 m (Figure

30; section A2). The resistivity values within the transect ranged from 0.47 to 8.26 Ωm. The most resistive values were found on top of the lagoon sediment with values between 3.0 and 8.26 Ωm. Under this resistive zone was a ~15 m-thick conductive region with an average resistivity of 1 Ωm. The conductive zone persisted even in the less resolvable deeper areas of the lagoon sediment profile (i.e., the more transparent areas in Figure 30; section A2).

An underwater ERI survey was conducted perpendicular to the beach in 2015 (Figure 30; transect B3). The shore-perpendicular transect was at a site where supra-permafrost groundwater seeps from a thaw slump feature on the tundra. This location was chosen to image whether this freshwater infiltrates into the lagoon sediment and how this is connected with ice-bonded permafrost distribution. Results of the underwater ERI survey placed perpendicular to the beach (transect B3 in 2015) showed a range of resistivities from 0.6 to 35 Ωm. There is a local resistive plume juxtaposed on top of a saline conductive region closest to the shore. The rest of the resistivity distribution is homogeneous and averages to 2.5 Ωm, with most values <10 Ωm.

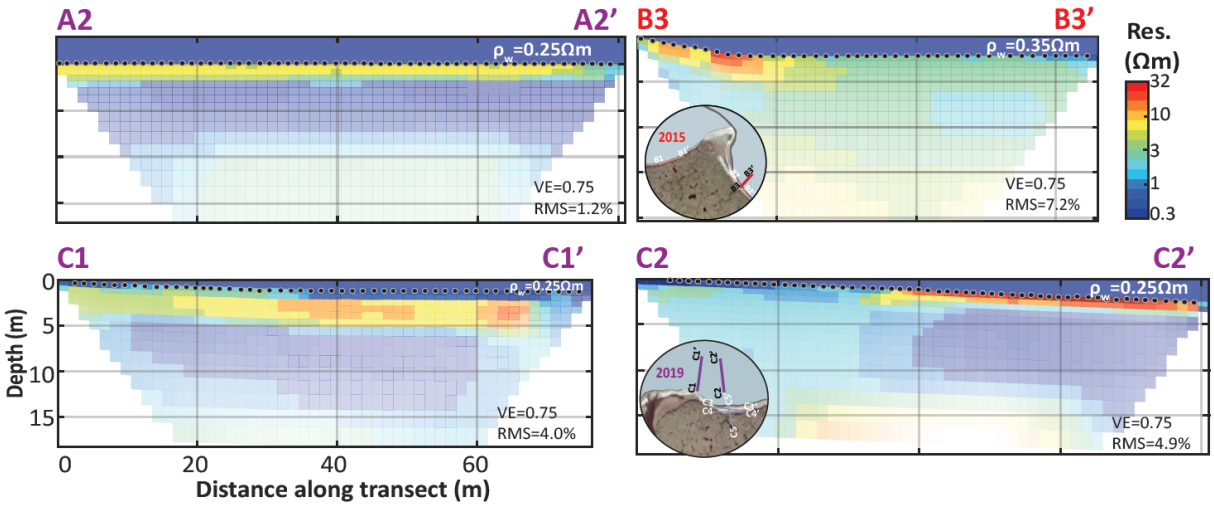

Figure 30: Inverted tomograms for underwater electrical resistivity surveys. The color intervals are logarithmic and the model resolution of each block is denoted by its transparency. Fixed water layer resistivity was assumed in the inversion and the resulting root mean square (RMS) error and vertical exaggeration (VE) is shown for each inversion. The location of survey transects are indicated in the inset maps. Note that line A2-A2' is located in the middle of the lagoon (see Figure 28 for location).

Two more underwater ERI surveys were conducted in 2019; one (C2) was orthogonal to land surveys and another (C1) was about ~75 m to the west of line C2 (Figure 29). Both underwater profiles were not in an area directly adjacent to a thaw slump feature, such as transect B3. These submarine surveys were done to investigate the presence or absence of ice-bonded permafrost deep without the complexity brought about by freshwater seeps. Results from the underwater ERI C2 transect showed conductive values between 1 and 3 Ωm for the first 30 m nearshore and a thin resistive layer on top with values ~ 10 Ωm offshore. These results were similar to transect A2, which was carried out in the middle of the

lagoon. Below the resistive layer, the subsurface was homogeneous and divided into two main resistivity distributions: a 30 m-wide zone with resistivity of 3 Ωm next to a zone with a resistivity of 0.5 Ωm. These zones show conductivity increasing away from shore. Results from the underwater ERI line C1 showed a similar pattern with a thin 1 m conductive layer on top of the more resistive ~2.5 m layer across the entire transect. Below the resistive layer, the subsurface is homogeneous and conductive with resistivities < 1 Ωm.

4.2 ELECTRICAL RESISTIVITY PROFILES AT THE SHORE

Terrestrial ER surveys, where electrodes were buried at the beach/soil surface, were also conducted in the summers of 2015 and 2019 to image the coasts. The first surveys were in a southeastern section and the latter surveys were to the southwest of the lagoon. Results from both the terrestrial ER transects B1 and B2 (in the southeastern field site) exhibited increasing resistivity with depth, from the water resistivity of 0.35 Ωm at the surface to 250 Ωm near the bottom of the profiles (Figure 31). Resistive zones (~200 Ωm) were present above 5 m depth; patches of relatively lower resistivity were present in these shallow areas. The deeper parts of the profiles, below ~7 m depth, were uniformly conductive although the resolution is limited.

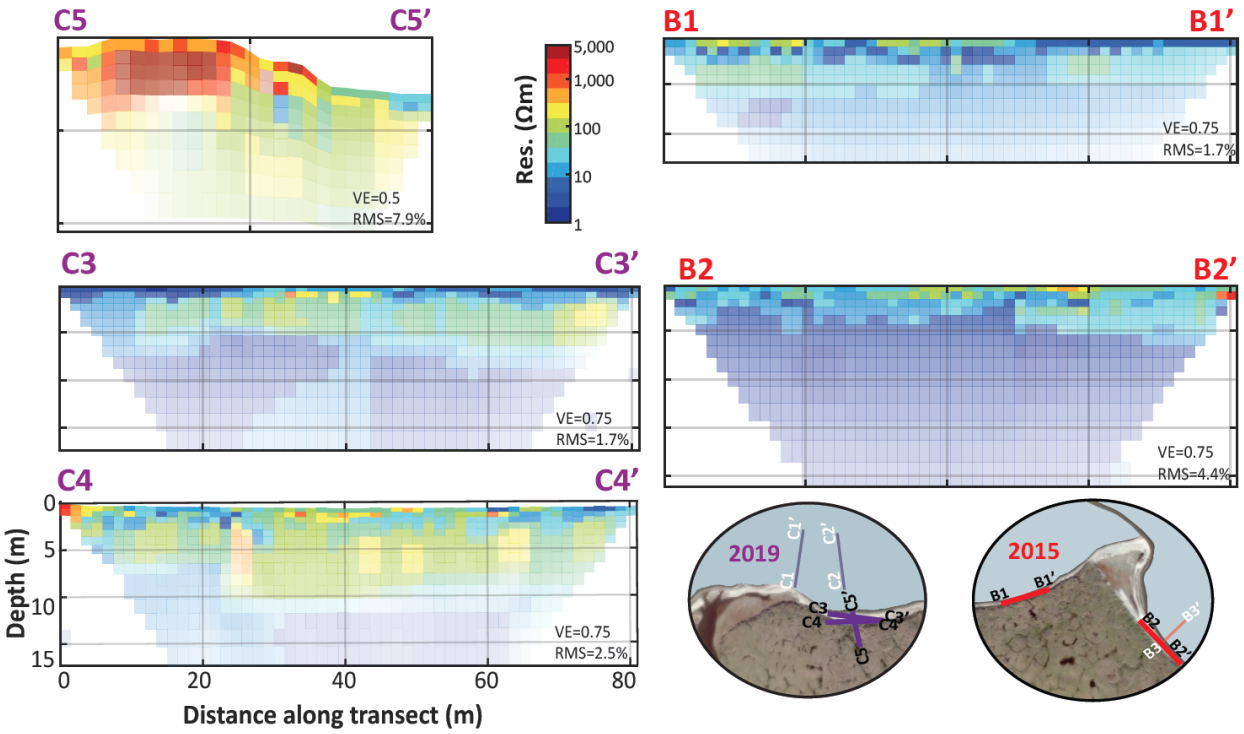

Figure 31: Inverted tomograms for terrestrial electrical resistivity surveys. The color intervals are logarithmic and the model resolution of each block is denoted by its transparency. The resulting root mean square (RMS) error and vertical exaggeration (VE) is shown for each inversion. The location of survey transects are indicated in the inset maps.

Several surveys were conducted at the southwestern coast field site (Figure 32). We conducted a survey right along the shoreline (C3), similar to transects B1 and B2 from the southeastern side, and an additional shore-parallel survey (C4) but right next to the tundra. Results from the southwestern shore field site (C3 and C4) revealed a resistive area along the shore that did not extend deeper than 7 m (Figure 31; see C3). This resistive zone extends deeper to ~11 m next to the tundra-beach transition (Figure 31, see C4), with an average resistivity

of ~200 Ωm and similar pattern to the eastern land surveys made in 2015 (B1 and B2). Below the shallow resistive area, the subsurface was conductive and fairly homogeneous.

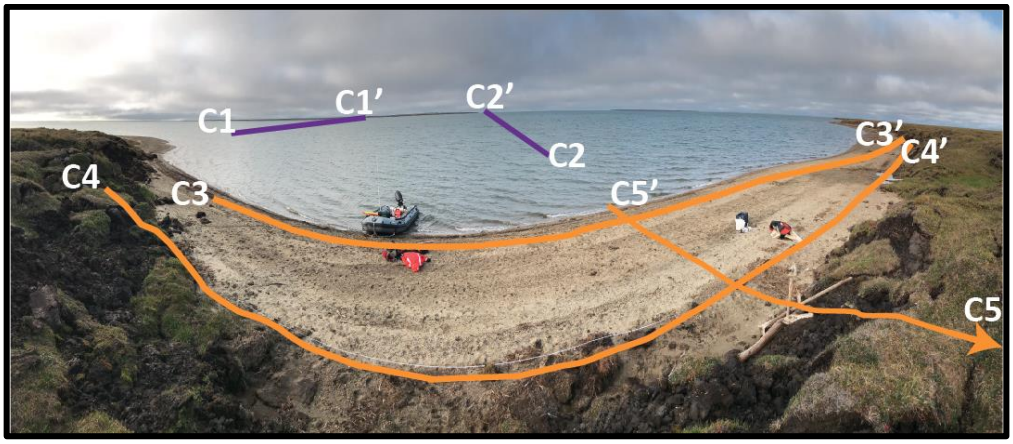

Figure 32: Panoramic view of ER surveys in the southwestern coast field site.

An orthogonal survey (C5) crossing survey lines C3 and C4 from the shoreline towards the tundra with about half covering the beach and the other half covering ice wedge-polygons was also conducted. This transect went across a high-centered ice-wedge polygon where ice-bonded permafrost was found at 30 cm depth. The transect allowed for constraining the method with known frozen sediment and for mapping the distribution of the ice-bonded permafrost distribution going from the tundra towards the beach (Figure 31). The resistivity distribution from the orthogonal survey running perpendicular to the shoreline towards the tundra (C5, which crosses lines C3 and C4) varied over five orders of

magnitude, ranging from less than 1 Ωm to over 10,000 Ωm (Figure 31). The most conductive areas were found in the shallow zone near the shoreline as would be expected. However, there were some conductive areas below the highly resistive regions for the entire profile. These resistive values ranged between 1,000 and 10,000 Ωm and did not extend deeper than ~3.5 m. Although not fully resolved, the deeper subsurface below the resistive 3.5 m-thick layer had resistivity values ranging from 10 Ωm to < 200 Ωm. The higher resistive values near 200 Ωm sloped downwards towards the shore.

If we compare the resistivity distribution of transects C4, on the beach next to the tundra, and C5, perpendicular to the tundra, we can observe that both ERI surveys show a trend of decreasing resistivity with depth, regardless of the horizontal location (Figure 33). This is, once again, suggestive of unfrozen sediment below the 3-4 m depths.

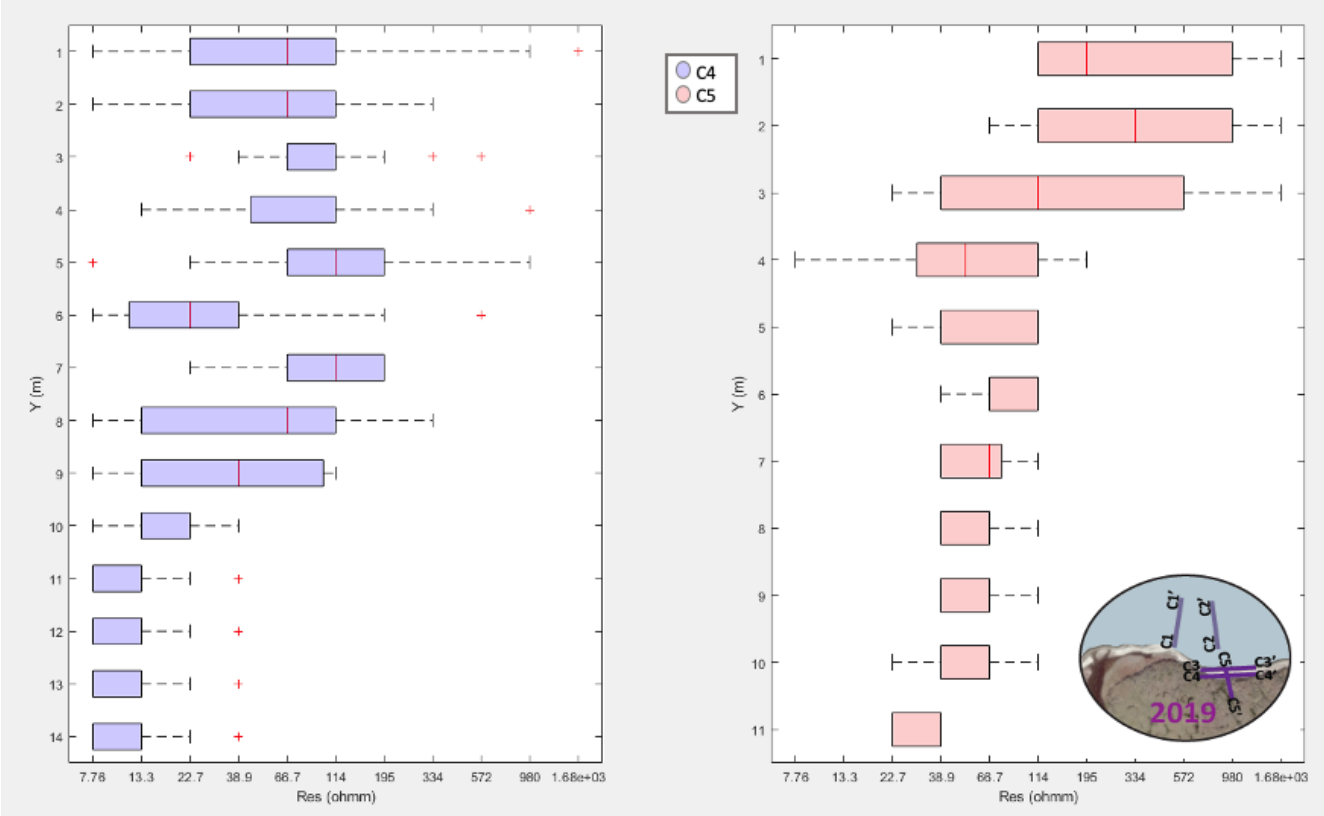

Figure 33: Depth (y)-binned comparison of C4 and C5 resistivity profiles shows a decreasing resistivity ranges with depth regardless of the electrode position in the surface.

Chapter 5: Discussion and Conclusions

5.1 IMPLICATIONS

Unfrozen sediment that is water saturated provides a conduit for electrical current through the pores, and higher salinity as well as clay content enhances its capacity to transmit current (Fortier, Allard, & Seguin, 1994). In contrast, frozen sediment with significant ice content resists passage of current. We expect frozen sediment to have exponentially higher resistivities than unfrozen sediment and we expect to find frozen sediment deeper in the subsurface at much lower thermal regimes.

The bulk ER of subsurface materials depends on both the solid matrix (i.e., its composition, texture and porosity) and the material filling the voids. Freshwater usually ranges between 10 – 500 Ωm whereas sea water will remain below 1 Ωm (Kasprzak et al., 2017). The overlying water column is electrically conductive during summer with resistivity values ranging between 0.2 and 0.5 Ωm for 2011-2014, precluding the possibility that the top sediment porewater is fresh (Harris et al., 2017). In August, when the surveys were conducted, surface and bottom water temperatures ranged between 10°C to 11°C (typical for Beaufort Sea lagoons) likely preventing the freezing of the top sediment layer and ruling out the presence of ice in the shallow depths of the underwater profiles (Harris et al., 2017). Surficial sediment samples collected near section C2 ranged in size from that of silt to gravel, but in some cases both sediment class sizes were

found together. Thus, the high resistivity values observed in the top few meters of sections C1, C2, and most likely A2, are indicative of a sedimentological change from resistive gravel and sands to more conductive silts and even muds rather than a pore fluid phase change. The very low resistivity observed throughout the underwater ER surveys from Kaktovik Lagoon with ER <10 Ωm at significant depths (Figure 30), suggests that the area encompassing the middle of the lagoon is free of ice-bonded permafrost down to at least 17 m within the lagoon sediment.

The tomograms of the terrestrial ER surveys along the beach had resistivity values <1,000 Ωm for all surveys except C5 and the first two electrodes of C4. Given the ~10 m spacing between the relatively parallel lines C3 and C4, we can assume that the lithology (porosity and tortuosity) and saturation extent remains more or less uniform. Observations of the lithology made by digging shallow holes on the beach supports this assertion. Therefore, the increase in shallow resistivity closer to the tundra is attributed to a difference in pore water salinity (compare the parallel lines C3 and C4 in Figure 31). This suggests that there exists an annulus of fresher water along the lagoon coast derived from the tundra. Our resistivity measurement from beneath the beach matches more closely with freshwater extracted from the channel between ice-wedge polygons (43 Ωm) than lagoon water (0.35 Ωm), thereby further supporting groundwater along the beach is sourced from the tundra where elevation is also higher, inducing an elevation head gradient. The shallow (topmost) resistive areas in the tomograms

roughly coincided with where fresher water sample was observed in co-located holes (Figure 19). The only possible source of this fresh water is the supra-permafrost zone (or active layer) on land. This water may be delivered as direct subsurface seepage or as channelized flows from the polygon troughs. The channels draining the polygons were found to sometimes drain directly into the lagoon (e.g., the channel shown in Figure 18), disappear and infiltrate into the beach sediment, or form puddles (see top of picture in Figure 18; transects C3 and C4 end at this puddle). We surmise that these freshwater bodies and conveyors intermittently transition from one state to the other, depending on tidal, wave, and hydro-climatic conditions.

Nearer to the lagoon water line, resistivity decreased towards that typical of saline water-saturated unfrozen sediment. The only tomogram that indicated extensive ice-bonded permafrost is line C5, which started on the tundra, cut across a high-centered ice-wedge polygon, and then continued to the beach until the water line. In this transect, the ice is obvious with a strong contrast between unfrozen and frozen material with an ER >1,000 Ωm and reaching values > 10,000 Ωm. The frost table was detected at around 30 cm depth in the polygon. Interestingly, this transect captured the ice disappearing at the beach and also under the polygon. Ice was also detected at the edge of C4; the first electrode of C4 (to the west; see Figure 30) was placed on top of the coastal bluff where probing showed ice.

Forward modeling was conducted in order to interpret C5 and evaluate if ER can discriminate between vertically continuous and shallow ice (Figure 27). The results of this analysis indicate that the low resistivity region under the frozen zone of the ice-wedge polygon is not an artifact of the ER survey design or the post-processing. The inverted tomograms of the field ER surveys are consistent with the absence of ice or frozen sediment under the polygon.

The resistivities are not reflective of ice or ice-bonded permafrost (Angelopoulos et al., 2019; Hubbard et al., 2013; Kasprzak et al., 2017; Overduin et al., 2012; Overduin et al., 2016; Sellmann et al., 1989; Swarzenski et al., 2016; Kenji Yoshikawa, Romanovsky, Duxbury, Brown, & Tsapin, 2004). The absence of ice-bonded permafrost within the lagoon and along the coast, even below the known ice in the case of transect C5, implies that the unfrozen, water-saturated substrate under the lagoon continues under the 3.5m thick ice-bonded permafrost body (Figure 34).

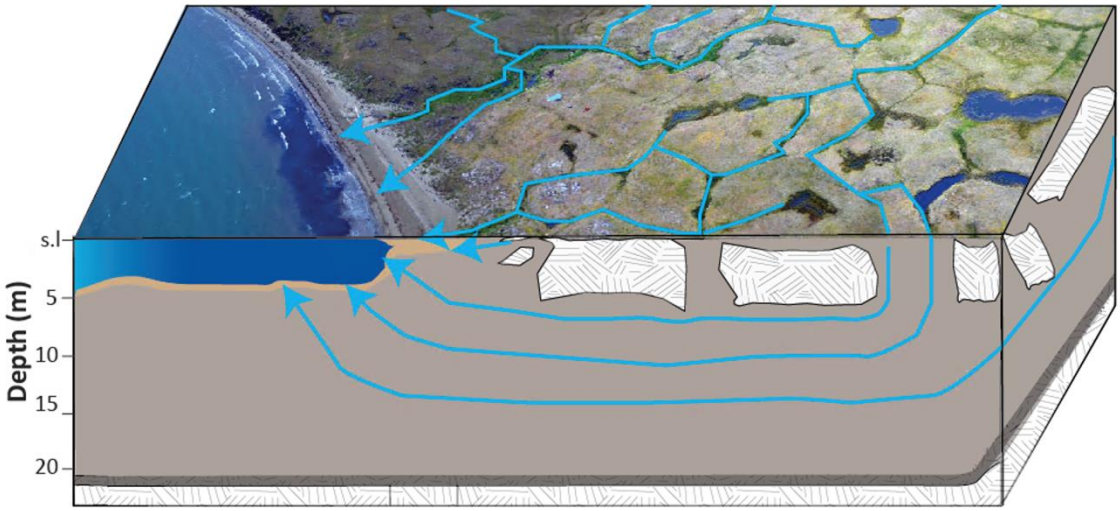

Figure 34: Conceptual model of surface water and groundwater entering Kaktovik lagoon. Both waters carrying dissolved carbon and nutrients. Groundwater is transported underneath the thin ice bonded permafrost and through the active layer.

This talik is expected to have dynamic hydrogeologic flow and transport processes similar to that of coastal aquifers in low-latitude areas (Figure 35). The freshwater movement from the tundra towards the beach helps explain why Kaktovik Lagoon has an overall trend of increasing resistivity between 2011 and 2014 (Harris et al., 2017).

A ~20m deep extensive talik suggests one of three hypotheses. First, there was not any ice to begin with in the deeper subsurface but rather it represents cryopeg material, essentially a high salinity talik, which was never frozen due to the freezing point depression of hypersaline silty clay. This would be similar to resistivity observations (8-20 Ωm) from the brine in Barrow, Alaska (Kenji

Yoshikawa et al., 2004). Second, the ice imaged in the ice-wedge polygons which would have extended into and through the lagoon has thawed abruptly, resulting in land subsidence, which is controlled by timing that is difficult to monitor (Walter Anthony et al., 2018). Third, the ice has been continually thawing at a relatively fast rate over long periods of time. That is, the thaw front is more or less at the coast all the time. Our results cannot constrain which one is the most likely explanation for the talik, emphasizing the need for time series observations. Regardless of the driving mechanism, our study reveals that there is an extensive talik across the entire lagoon connected to a sub-permafrost aquifer where saline groundwater flow mixes with freshwater from thawing ice polygons and incoming freshwater channels. We acknowledge that the extent, depth, and amount or degree of this mixture is unknown and requires further investigation. Nonetheless, whatever organic matter is in the aquifer/lagoon sediment is now liberated and free to react and escape as gases or be transported as dissolved organic matter. In fact, measurements of groundwater tracers in the lagoon indicate that supra-permafrost groundwater flow has abundant dissolved organic matter and nutrients. These could be mineralized and released as carbon dioxide or methane or incorporated into lagoon biota, thereby providing a source of energy for lower trophic productivity in the lagoons (Connolly et al., 2020). These processes may be critical when considering the hydrologic, biogeochemical, and ecological functioning of the lagoon system.

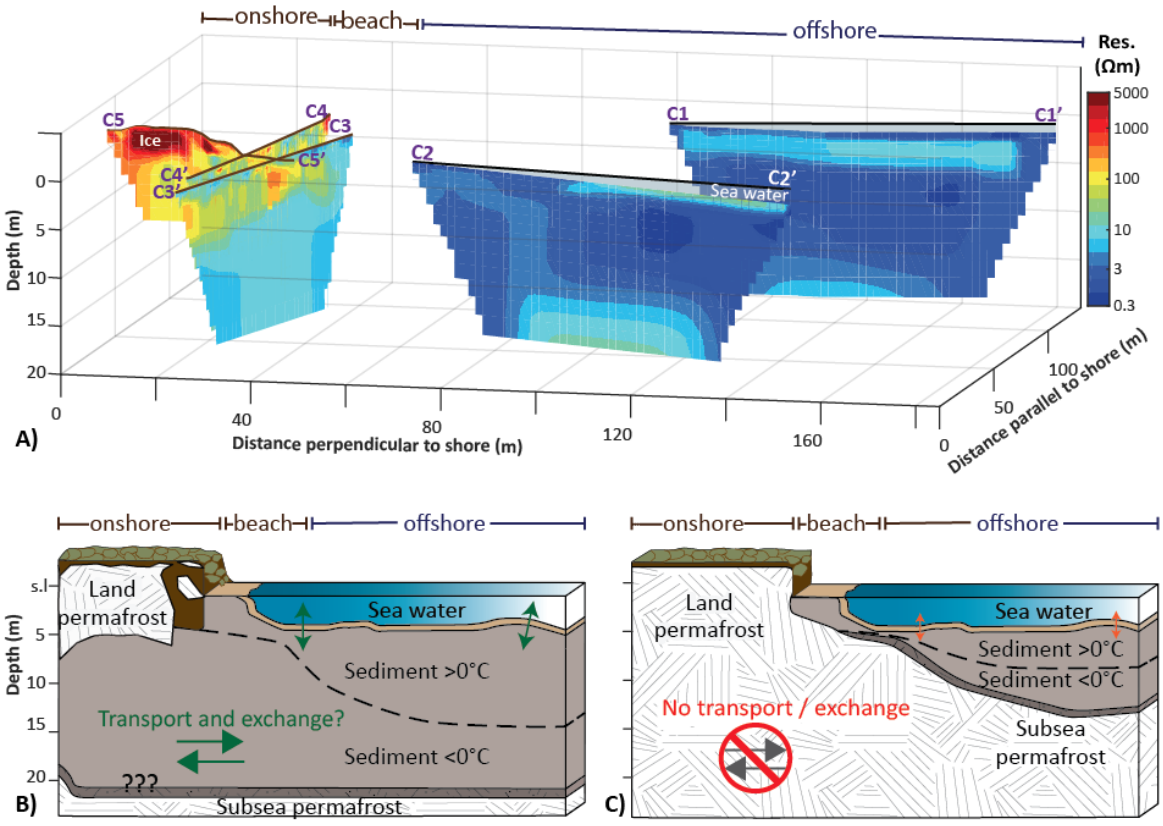

Figure 35: Conceptual models. (A) shows the interpolated field data tomograms acquired in 2019 from the southwestern site (C transects) without controlling the transparency. (B) shows a conceptual interpretation following (A) where there is an extensive talik under the lagoon and the beach beneath a shallow ice patch. The talik possibly extends further in-land through connection with a potential cryopeg (C) shows the prevailing conceptual model for shallow subsea ice-bonded permafrost connected to terrestrial ice-bonded permafrost.

Electrical resistivity imaging provides an excellent tool for determining the extent of the thawed sediment and likewise the depth to frozen permafrost across the land to lagoon interface. Monitoring potential changes in subsurface ice-bonded permafrost can provide very valuable information on whether frozen

sediment is thawing across this interface, which can then be related to changes in other measurements (such as salinity, temperature, erosion, organic matter, nutrients, and chlorophyll) to comprehensively connect climate change and its effect on the hydrology, biogeochemistry and ecology of lagoon ecosystems in the Arctic.

5.2 CONCLUSIONS

Very low resistivity (<10 Ωm) observed in the lagoon at significant depths ~17 m and low resistivity (<200 Ωm) observed on land at even greater depths ~22 m, suggests that the lagoon subsurface is devoid of ice-bonded permafrost down to those depths. Resistive anomalies at the surface of the beach (>150 Ωm) and at depth increasing with distance away from the shore indicate freshwater seeping into the lagoon and mixing with the denser saltwater. Future directions include field validation of the absence of ice-bonded permafrost via borehole temperature and salinity measurements, drilling of sediment cores and predicting the rate of ice-bonded permafrost thaw using erosion rates and insitu borehole temperature measurements.

Bibliography

Angelopoulos, M., Westermann, S., Overduin, P., Faguet, A., Olenchenko, V., Grosse, G., & Grigoriev, M. N. (2019). Heat and salt flow in subsea permafrost modeled with CryoGRID2. *Journal of Geophysical Research: Earth Surface, 124*(4), 920-937. doi: 10.1029/2018jf004823

Brothers, L. L., Herman, B. M., Hart, P. E., & Ruppel, C. D. (2016). Subsea ice-bearing permafrost on the U.S. Beaufort Margin: 1. Minimum seaward extent defined from multichannel seismic reflection data. *Geochemistry, Geophysics, Geosystems, 17*(11), 4354-4365. doi: doi:10.1002/2016GC006584

Bruggeman, D. A. G. (1935). Berechnung verschiedener physikalischer Konstanten von heterogenen Substanzen. I. Dielektrizitätskonstanten und Leitfähigkeiten der Mischkörper aus isotropen Substanzen. *Annalen der Physik, 416*(7), 636-664. doi: 10.1002/andp.19354160705

Cardenas, M. B., Zamora, P. B., Siringan, F. P., Lapus, M. R., Rodolfo, R. S., Jacinto, G. S., . . . Senal, M. I. (2010). Linking regional sources and pathways for submarine groundwater discharge at a reef by electrical resistivity tomography,222Rn, and salinity measurements. *Geophysical Research Letters, 37*(16). doi: 10.1029/2010gl044066

Castro, J., Ballesteros, F., Méndez, A., & Tarquis, A. M. (2014). Fractal Analysis of Laplacian Pyramidal Filters Applied to Segmentation of Soil Images. *TheScientificWorldJournal, 2014*, 212897. doi: 10.1155/2014/212897

Connolly, C. T., Cardenas, M. B., Burkart, G. A., Spencer, R. G. M., & McClelland, J. W. (2020). Groundwater as a major source of dissolved organic matter to Arctic coastal waters. *Nature Communications, 11*(1), 1479. doi: 10.1038/s41467-020-15250-8

Cuomo, C. J., Eisner, W., & Hinkel, K. (2008). Environmental change, indigenous knowledge, and subsistence on Alaska's North Slope. *The Scholar and Feminist Online*(7.1).

D. Jackson, P., Taylor Smith, D., & N. Stanford, P. (1978). *Resistivity-porosity-particle shape relationships for marine sands* (Vol. 43).

Day-Lewis, F. D., Singha, K., & Binley, A. M. (2005). Applying petrophysical models to radar travel time and electrical resistivity tomograms: Resolution-dependent limitations. *Journal of Geophysical Research: Solid Earth, 110*(B8). doi: 10.1029/2004jb003569

Dunton, K. H., Schonberg, S. V., & Cooper, L. W. (2012). Food web structure of the Alaskan nearshore shelf and estuarine lagoons of the Beaufort Sea. *Estuaries and Coasts, 35*(2), 416-435. doi: 10.1007/s12237-012-9475-1

Fortier, R., Allard, M., & Seguin, M. K. (1994). Effect of physical properties of frozen ground on electrical resistivity logging. *Cold Regions Science and Technology, 22*(4), 361-384. doi: https://doi.org/10.1016/0165-232X(94)90021-3

Fortier, R., LeBlanc, A.-M., Allard, M., Buteau, S., & Calmels, F. (2008). Internal structure and conditions of permafrost mounds at Umiujaq in Nunavik, Canada, inferred from field investigation and electrical resistivity tomography. *Canadian Journal of Earth Sciences, 45*(3), 367-387. doi: 10.1139/E08-004

Fritz, M., Vonk, J. E., & Lantuit, H. (2017). Collapsing Arctic coastlines. *Nature Climate Change, 7*(1), 6-7. doi: 10.1038/nclimate3188

Gibbs, A. E., Nolan, M., Richmond, B. M., Snyder, A. G., & Erikson, L. H. (2019). Assessing patterns of annual change to permafrost bluffs along the North Slope coast of Alaska using high-resolution imagery and elevation models. *Geomorphology, 336*, 152-164. doi: https://doi.org/10.1016/j.geomorph.2019.03.029

Gibbs, A. E., & Richmond, B. M. (2017). National assessment of shoreline change—Summary statistics for updated vector shorelines and associated shoreline change data for the north coast of Alaska, U.S.-Canadian Border to Icy Cape *Open-File Report* (pp. 21). Reston, VA.

Harris, C. M., McClelland, J. W., Connelly, T. L., Crump, B. C., & Dunton, K. H. (2017). Salinity and Temperature Regimes in Eastern Alaskan Beaufort Sea Lagoons in Relation to Source Water Contributions. *Estuaries and Coasts, 40*(1), 50-62. doi: 10.1007/s12237-016-0123-z

Hauck, C. (2013). New Concepts in Geophysical Surveying and Data Interpretation for Permafrost Terrain. *Permafrost and Periglacial Processes, 24*(2), 131-137. doi: doi:10.1002/ppp.1774

Hoekstra, P. (1973). Electromagnetic probing of permafrost. *Proceedings of 2nd International Conference on Permafrost, Yakutsk, USSR, North American Contribution*, 517-526.

Hubbard, S. S., Gangodagamage, C., Dafflon, B., Wainwright, H., Peterson, J., Gusmeroli, A., . . . Wullschleger, S. D. (2013). Quantifying and relating land-surface and subsurface variability in permafrost environments using LiDAR and surface geophysical datasets. *Hydrogeology Journal, 21*(1), 149-169. doi: 10.1007/s10040-012-0939-y

Hugelius, G., Strauss, J., Zubrzycki, S., Harden, J. W., Schuur, E. A. G., Ping, C. L., . . . Kuhry, P. (2014). Estimated stocks of circumpolar permafrost carbon with quantified uncertainty ranges and identified data gaps. *Biogeosciences, 11*(23), 6573-6593. doi: 10.5194/bg-11-6573-2014

Kasprzak, M., Strzelecki, M. C., Traczyk, A., Kondracka, M., Lim, M., & Migała, K. (2017). On the potential for a bottom active layer below coastal permafrost: the impact of seawater on permafrost degradation imaged by electrical resistivity tomography (Hornsund, SW Spitsbergen). *Geomorphology, 293*, 347-359. doi: https://doi.org/10.1016/j.geomorph.2016.06.013

Lindgren, A., Hugelius, G., Kuhry, P., Christensen, T. R., & Vandenberghe, J. (2016). GIS-based maps and area estimates of northern hemisphere permafrost extent during the Last Glacial Maximum. *Permafrost and Periglacial Processes, 27*(1), 6-16. doi: 10.1002/ppp.1851

Loke, M. (2011). *Electrical Resistivity Surveys and Data Interpretation*.
Loke, M. H., & Barker, R. D. (1996). Rapid least-squares inversion of apparent resistivity pseudosections by a quasi-Newton method1. *Geophysical Prospecting, 44*(1), 131-152. doi: doi:10.1111/j.1365-2478.1996.tb00142.x
Moore, J. C., Grinsted, A., Zwinger, T., & Jevrejeva, S. (2013). Semiempirical and process-based global sea level projections. *Reviews of Geophysics, 51*(3), 484-522. doi: 10.1002/rog.20015
Mu, C., Zhang, T., Abbott, B. W., Wang, K., Ge, S., Sayedi, S. S., . . . Peng, X. (2019). Organic carbon pools in the subsea permafrost domain since the Last Glacial Maximum. *Geophysical Research Letters, 46*(14), 8166-8173. doi: 10.1029/2019gl083049
Olhoeft, G. (1975). *The electrical properties of permafrost*.
Osterkamp, T. E. (2001). Subsea permafrost *Encyclopedia of ocean sciences* (Vol. 5, pp. 2902-2912): Elsevier.
Osterkamp, T. E., & Jorgenson, J. C. (2006). Warming of permafrost in the Arctic National Wildlife Refuge, Alaska. *Permafrost and Periglacial Processes, 17*(1), 65-69. doi: 10.1002/ppp.538
Overduin, P. P., Westermann, S., Yoshikawa, K., Haberlau, T., Romanovsky, V., & Wetterich, S. (2012). Geoelectric observations of the degradation of nearshore submarine permafrost at Barrow (Alaskan Beaufort Sea). *Journal of Geophysical Research: Earth Surface, 117*(F2). doi: doi:10.1029/2011JF002088
Overduin, P. P., Wetterich, S., Günther, F., Grigoriev, M. N., Grosse, G., Schirrmeister, L., . . . Makarov, A. (2016). Coastal dynamics and submarine permafrost in shallow water of the central Laptev Sea, East Siberia. *The Cryosphere, 10*(4), 1449-1462. doi: 10.5194/tc-10-1449-2016
Pearson, C. F., Halleck, P. M., McGuire, P. L., Hermes, R., & Mathews, M. (1983). Natural gas hydrate deposits: a review of in situ properties. *The Journal of Physical Chemistry, 87*(21), 4180-4185. doi: 10.1021/j100244a041
Ruppel, C. D., & Kessler, J. D. (2017). The interaction of climate change and methane hydrates. *Reviews of Geophysics, 55*(1), 126-168. doi: doi:10.1002/2016RG000534
Scott, W., & Kay, A. E. (1988). *Earth resistivities of Canadian soils*: Canadian Electrical Association.
Scott, W. J., Sellmann, P. V., & Hunter, J. A. (1978). 13. Geophysics in the Study of Permafrost *Geotechnical and Environmental Geophysics: Volume I, Review and Tutorial* (pp. 355-384).
Sellmann, P. V., Delaney, A. J., & Arcone, S. A. (1989). Coastal subsea permafrost and bedrock observations using dc resistivity. Hanover NH: Cold Regions Research and Engineering Lab
Shakhova, N., Semiletov, I., Gustafsson, O., Sergienko, V., Lobkovsky, L., Dudarev, O., . . . Chernykh, D. (2017). Current rates and mechanisms of subsea permafrost degradation in the East Siberian Arctic Shelf. *Nature Communications, 8*, 15872. doi: 10.1038/ncomms15872

Swarzenski, P. W., Johnson, C. D., Lorenson, T. D., Conaway, C. H., Gibbs, A. E., Erikson, L. H., . . . Waldrop, M. P. (2016). Seasonal electrical resistivity surveys of a coastal bluff, Barter Island, North Slope Alaska. *Journal of Environmental & Engineering Geophysics, 21*(1), 37-42. doi: 10.2113/jeeg21.1.37

Vanhala, H., Lintinen, P., & Ojala, A. (2009). *Electrical resistivity study of permafrost on Ridnitšohkka fell in Northwest Lapland, Finland* (Vol. 45).

Walter Anthony, K., Schneider von Deimling, T., Nitze, I., Frolking, S., Emond, A., Daanen, R., . . . Grosse, G. (2018). 21st-century modeled permafrost carbon emissions accelerated by abrupt thaw beneath lakes. *Nature Communications, 9*(1), 3262. doi: 10.1038/s41467-018-05738-9

Wendler, G., Shulski, M., & Moore, B. (2010). Changes in the climate of the Alaskan North Slope and the ice concentration of the adjacent Beaufort Sea. *Theoretical and Applied Climatology, 99*(1), 67-74. doi: 10.1007/s00704-009-0127-8

Wu, Y., Hubbard, S. S., Ulrich, C., & Wullschleger, S. D. (2013). Remote Monitoring of Freeze–Thaw Transitions in Arctic Soils Using the Complex Resistivity Method. *Vadose Zone Journal, 12*(1), vzj2012.0062. doi: 10.2136/vzj2012.0062

Yoshikawa, K., Leuschen, C., Ikeda, A., Harada, K., Gogineni, P., Hoekstra, P., . . . Matsuoka, N. (2006). Comparison of geophysical investigations for detection of massive ground ice (pingo ice). *Journal of Geophysical Research: Planets, 111*(E6). doi: 10.1029/2005je002573

Yoshikawa, K., Romanovsky, V., Duxbury, N., Brown, J., & Tsapin, A. (2004). The Use of Geophysical Methods to Discriminate between Brine Layers and Freshwater. *J Glaciol Geocryol, 26*, 301-309.